Analysis of Passive Tracer Transport as Modeled by an Atmospheric General Circulation Model

MARK HOLZER

Canadian Centre for Climate Modelling and Analysis, Atmospheric Environment Service, University of Victoria, Victoria, British Columbia, Canada

ABSTRACT

Tracers without feedback on the atmosphere are used to probe tropospheric transport. Such passive tracers are considered for two important anthropogenic sources, Europe and eastern North America. The linearity of passive tracer continuity allows transport to be formulated in terms of a Green function, G. A coarse-grained Green function is defined that is suitable for numerical investigation with a GCM. An ensemble of independent realizations of the atmosphere is used to obtain the model's ensemble mean, or "climate" Green function. With increasing time, the individual realizations of G converge to their climate mean and this convergence is quantified in terms of the decay of ensemble fluctuations. Throughout, G is analyzed with the goal of gaining new insight into the tracer climate that results from constant sources.

The climate Green function is used to identify transport timescales, pathways, and mechanisms. The Green function is zonally mixed after about 3 months. The time to mix G to within 10% of its asymptotic value exceeds 1 yr at high-latitude lower levels, while the interhemispheric two-box exchange time is ~7 months. Tracers from Europe and eastern North America follow different pathways with distinct seasonality. Eddies play a key role in transport. Transport in the Southern Hemisphere is dominated by transient eddies resulting from tracer injected ~4 months earlier. These transient eddies extend throughout much of the troposphere, and align to a large degree with contours of zonally averaged mixing ratio. Large seasonal changes of the mean-motion part of the tracer flux are primarily compensated by the standing-eddy transport. Ensemble fluctuations of G decay with an approximate t^{-3} power law. Eddy conversion provides a source of fluctuations, while dissipation damps ensemble fluctuations with a timescale of ~10 days. In the GCM context, the relative importance of parameterized versus resolved vertical transport is examined.

1. Introduction

Trace gases, or simply "tracers," are an important part of the global climate system. Concentrations of inert long-lived tracers such as SF_6 and C_2F_6 are easily measured and provide valuable information on atmospheric transport and mixing (e.g., Harnisch et al. 1996). Deviations of CO_2 from the well-mixed global mean may to first order be considered as inert tracers whose distribution and seasonality gives important constraints on the biosphere (e.g., Fung et al. 1983). Other tracers, such as CH_4, form an important part of the tropospheric chemical budget and affect the radiation balance (Prather 1996). In fact, through their interactions with the biosphere, chemical cycles, and radiation, tracers may ultimately play a key role in determining the habitability of the planet (Prather 1996). An integral part of any

study of atmospheric tracers is a model and some understanding of atmospheric transport. For known sources, transport determines the spatial and temporal structure of the concentrations, for known concentrations and transport operator one has constraints on the sources (e.g., Enting et al. 1995, and references therein), and for known sources and a partial knowledge of the concentration, one can constrain the transport operator. Tracer transport properties cannot be deduced solely from the mean circulation, but depend on subtle aspects of the flow, such as the eddy fields, Lagrangian statistics, and, for a model, on the parameterized subgrid transport. In this paper, we focus on the problem of known sources of passive tracers, which get transported by the atmosphere, but which do not couple to any meteorological field and hence have no feedback on their transport operator. We can, therefore, use passive tracers as a direct, noninvasive probe of atmospheric transport.

The subject of turbulently advected passive tracers has a venerable history in the physics of fluids (e.g., Corrsin 1951; Kraichnan 1966, 1974), but continues to be of active experimental and theoretical interest (e.g., Gollub et al. 1991; Schraiman and Siggia 1994). In the

Corresponding author address: Dr. Mark Holzer, Canadian Centre for Climate Modelling and Analysis, Atmospheric Environment Service, University of Victoria, P.O. Box 1700, Victoria, BC V8W 2Y2, Canada.
E-mail: Mark.Holzer@ec.gc.ca

context of the atmosphere, detailed studies of large-scale chaotic or turbulent mixing have largely been confined to two-dimensional models of transport in the stratosphere, where cross-isentropic transport is often neglected to a first approximation (e.g., Pierrehumbert and Yang 1993). In the very complex setting of the troposphere, the large-scale zonally averaged transport has been studied in some detail in the context of a two-dimensional (2D) model that parameterizes eddy transport via a general flux-gradient relation, extracted from a GCM (Plumb and Mahlman, 1987). This 2D model was used to illustrate large-scale advective–diffusive balances and quasi-universal characteristics of nearly homogenized "chemical equilibrium" states for long-lived tracers (Plumb and McConalogue 1988). Full three-dimensional (3D) models are also commonly used, but often transport is taken for granted once the model has been "calibrated" against climatological data, or a relatively sparse set of tracer observations such as those for ^{222}Rn and ^{85}Kr (e.g., Jacob et al. 1987) or CFCs (e.g., Prather et al. 1987). Recently, there has been some effort to reduce uncertainty in tracer transport through model intercomparison (e.g., Rayner and Law 1995; Jacob et al. 1997; Denning et al. 1997).

In this paper, we focus on the climatic properties of tropospheric passive tracer transport as represented by a GCM. Typically, tracers of importance to climate are in a statistically (cyclo-)stationary state with global-scale sources of constant, slowly varying, or cyclic time dependence. Such statistically stationary states make it difficult, if not impossible, to deduce specific transport pathways and mechanisms for tracer emitted at a given location and time. Here, we will exploit the fact that passive tracer transport is linear in the mixing ratio, which allows one to think in terms of a Green function from which the solution for a general source-sink field may be synthesized. The Green function, G, is of course nothing but the normalized time-evolving tracer distribution resulting from the injection of tracer at a point in space and time, and, in principle, for all such points of interest. The Green function is, therefore, a functional of the velocity field and hence a random variable itself. Recently, a functional path integral representation of this Green function for homogeneous isotropic turbulence has been used to elucidate the subtle dependence of turbulent tracer transport on the Lagrangian statistics of the strain field (Schraiman and Siggia 1994). While such powerful analytical techniques may eventually prove useful for specific atmospheric problems, the complicated tropospheric convection and diffusion processes, and the general nonhomogeneous, nonisotropic nature of the troposphere demand a more direct numerical approach.

Because of the strong functional dependence of G on the flow, one must consider the "climate" of G (estimated as the mean over several realizations of the flow) and a statistical description of the fluctuations around this mean state. The ensemble statistics of G can then be used to synthesize the ensemble statistics of mixing ratio from arbitrary sources. The numerical determination of G for all possible source locations is, of course, prohibitive. To keep the problem to manageable size, we confine ourselves to two source locations, Europe and eastern North America, which are of interest because they are highly industrialized and emit a large fraction of many anthropogenic tracers. While in the absence of spatial homogeneity we thereby concern ourselves with only the part of G that is relevant for these source locations, we retain the generality of arbitrary time dependence of the sources. To minimize Gibbs oscillations in the spectral GCM used, and to keep the size of the ensemble needed to study ensemble fluctuations to an absolute minimum, we define a coarse-grained G, which is essentially the point-source G convolved in time and space with functions of convenient form. Such a coarse-grained G is defined for each month of the year and each of the two locations considered, and obtained for an ensemble of three separate simulations. While this is a small ensemble, it is sufficient for the study of globally, or time and zonally, averaged ensemble variance, as our analysis below will show.

The ensemble of coarse-grained Gs is used to study systematically the basic structure and seasonality of the climate Green function in terms of transport timescales, pathways, and mechanisms. This allows for new insight into the statistically stationary state, which results from constant sources, since such a state is the rapidly convergent sum of appropriately time-lagged G's. In the GCM context, the relative importance of resolved versus parameterized tracer transport is quantified. We then consider the fundamental self-averaging of G, that is, the way in which individual realizations of G converge to their ensemble-mean climate as G is increasingly mixed throughout the atmosphere. Ensemble fluctuations are found to decay with a power law much as in turbulent diffusion. To the best of the author's knowledge, this is the first study of this phenomenon in the context of global-scale tropospheric transport.

2. The Green function for passive tracers

a. General properties of the Green function

A passive tracer has a continuity equation that is linear in the mass mixing ratio, χ. Formally

$$\partial_t \chi + \mathcal{T}(\chi) = S, \tag{1}$$

where $\partial_t \equiv \partial/\partial t$ and $\mathcal{T}$ is a linear transport operator representing advection and diffusion. The source, S, is considered to be interior to the atmosphere with χ satisfying zero-flux boundary conditions. The corresponding Green function, G, is then defined by replacing the general source, S, by a Dirac δ function in space and time:

$$(\partial_t + \mathcal{T})G(\mathbf{r}, t \,|\, \mathbf{r}', t') = \delta(\mathbf{r} - \mathbf{r}')\delta(t - t'). \tag{2}$$

In Eq. (2), $\mathbf{r}$ denotes a general 3D coordinate. Through-

out, we adopt pressure, p, as the vertical coordinate, so that $\mathbf{r} = (p/g, \mathbf{x})$, where $\mathbf{x}$ denotes a 2D horizontal coordinate (g is the acceleration of gravity). Thus, $\delta(\mathbf{r} - \mathbf{r}') = g\delta(p - p')\delta(\mathbf{x} - \mathbf{x}') = g\delta(p - p')\delta(\phi - \phi')\,\delta(\lambda - \lambda')/[a^2 \cos(\phi)]$ in conventional latitude, ϕ, longitude, λ, coordinates (a is the earth's radius). The corresponding 3D integration measure is a mass element denoted by $d^3r = d^2x\, dp/g = a^2 \cos(\phi)\, d\phi\, d\lambda\, dp/g$. From (2) it follows that the solution to (1) is the linear superposition

$$\chi(\mathbf{r}, t) = \int d^3r' G(\mathbf{r}, t | \mathbf{r}', 0)\chi(\mathbf{r}', 0)$$
$$+ \int_0^t dt' \int d^3r' G(\mathbf{r}, t | \mathbf{r}', t')S(\mathbf{r}', t'). \quad (3)$$

The first term represents the time-evolved initial condition, $\chi(\mathbf{r}, 0)$, which we assume to be zero here. Alternatively, we may consider t to be much longer than the time necessary to homogenize the initial condition to an uninteresting, structureless background. Note that (2) implies the normalization $\int G\, d^3r = 1$, so that G has dimensions of inverse mass.

In principle, the transport operator $\mathcal{T}$ represents only advection and molecular diffusion. However, a GCM has relatively coarse spatial resolution and the effect of small-scale transport must be parameterized as convection and effective eddy diffusion. We write for $\mathcal{T}$, appropriate for GCM diagnostics,

$$\mathcal{T}(\chi) = (\mathbf{v} \cdot \mathbf{\nabla} + \omega\partial_p)\chi - \mathcal{D}_H(\chi) - \mathcal{D}_V(\chi), \quad (4)$$

where in pressure coordinates the vertical "velocity" is $\omega \equiv dp/dt$ and (airmass) continuity takes the simple form $\mathbf{\nabla} \cdot \mathbf{v} + \partial_p\omega = 0$ ($\mathbf{v}$ is horizontal velocity; $\partial_p \equiv \partial/\partial_p$). The operators $\mathcal{D}_H$ and $\mathcal{D}_V$ represent transport due to unresolved, parameterized horizontal and vertical processes (eddy diffusion and convection), respectively. Because we assign all sources to S with zero-flux boundary conditions, the vertical integral of $\mathcal{D}_V$ vanishes.

While not an issue for the GCM used here, some transport schemes are numerically nonlinear (see, e.g., Rasch 1994, and references therein). Such nonlinearities must necessarily be weak enough so that, at least over appropriate time and/or spatial averages, solutions from different sources are to a good approximation additive as in (3). If this is not the case, these artificial nonlinearities invalidate the transport model and not the Green function approach.

It is useful to summarize some of the general physical properties of G, which are relevant here. It is often convenient to rewrite the time arguments of G in terms of the delay, or lag, time, $\xi \equiv t - t'$. However, because the atmosphere is not statistically stationary in time, nor spatially homogeneous, we must retain separate ξ and t', as well as separate $\mathbf{r}$ and $\mathbf{r}'$, arguments. Given an ensemble of G's with identical sources but different, independent realizations of the atmosphere, the G's will exhibit strong fluctuations around their ensemble av-

erage, or climatological mean, $\{G\}$, at least for small ξ. For long times after the initial injection, mixing ratio becomes homogenized over the entire atmosphere so that G has the limit $G_\infty \equiv 1/(\int d^3r)$; that is,

$$\lim_{\xi \to \infty} G(\mathbf{r}, t | \mathbf{r}', t - \xi) = \frac{1}{4\pi a^2 \langle p_s \rangle/g} = G_\infty, \quad (5)$$

where p_s is the surface pressure, and $\langle \dots \rangle$ denotes the global horizontal average. Thus, G_∞ is a natural scale for G.

We expect a gradual transition from the initial pulse experiencing strong ensemble fluctuations to an intermediate state that is "self-averaged," that is, not totally smeared out to G_∞, but with small ensemble fluctuations and a nontrivial spatial and temporal structure. In other words, as ξ increases, $G \to \{G\}$, where G becomes a good approximation to $\{G\}$ well before $\{G\} \sim G_\infty$. As part of the characterization of the fluctuations of G about its climate, $\{G\}$, the self-averaging, $G \to \{G\}$, will be quantified in terms of the decay of ensemble fluctuations.

In the climatological mean, the dependence on t' becomes periodic with a period of 1 yr, assuming the atmosphere is itself in a statistically cyclostationary state, where all ensemble means depend only on the time of year or season. Therefore, we can write $\{G\}$ as a Fourier series in the source time, t', with coefficients G_n as

$$\{G(\mathbf{r}, t' + \xi | \mathbf{r}', t')\}$$
$$= \sum_n \{G_n(\mathbf{r}, \mathbf{r}', \xi)\} \exp(i\omega_n t'), \quad (6)$$

where the only frequencies present are $\omega_n = 2\pi n/T$, with $T = 1$ yr and $n = 0, \pm 1, \pm 2, \dots$.

b. Practical limitations and considerations for numerical calculations

All GCM experiments were performed with the Canadian Climate Centre second generation GCM (CCC GCMII; McFarlane et al. 1992), which is a spectral model with triangular truncation at principle wavenumber 32 and 10 hybrid sigma-pressure vertical levels with an upper boundary at 10 mb. The tracer advection was performed spectrally without any hole filling. While this does not ensure positive definiteness of the mixing ratio at all times, the very accurate spectral transport is a bonus and the occasional Gibbs overshoot is not an impediment for a purely passive tracer. Parameterizations of unresolved tracer transport parallel those used for moisture.

Spectral methods are not designed to deal with the equivalent of a δ function on a grid whose large spatial gradients lead to considerable Gibbs oscillations. We deal with this difficulty by computing what is essentially a smoothed Green function. Instead of expanding the source, S, in δ functions, we expand in functions that have a smooth finite spatial extent. There is also a very
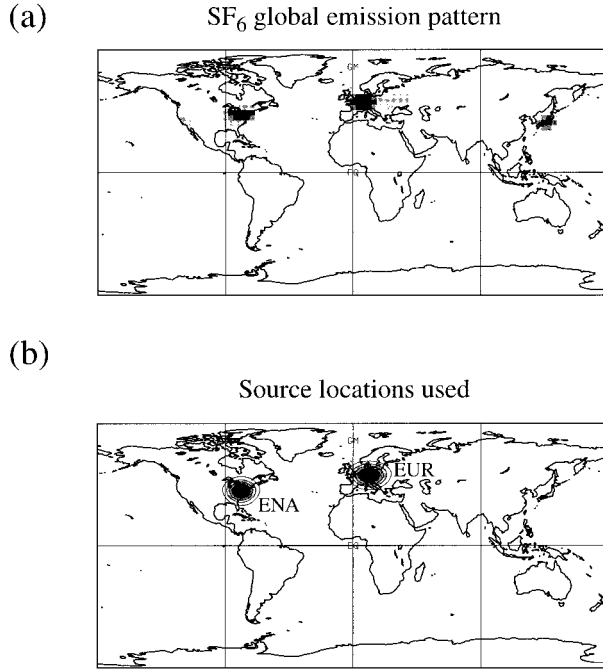
(a)

SF$_6$ global emission pattern

(b)

Source locations used

FIG. 1. (a) The emission pattern for SF$_6$ at the resolution of the GCM. The SF$_6$ sources are distributed according to electrical power usage (Levin and Hesshaimer 1996). (b) The EUR and ENA source patterns on the same linear grayscale as (a).

different kind of difficulty associated with localizing the source in time, namely, that of large ensemble variability. If the source is only "turned on" for a single time step (~20 min), the subsequent evolution of mixing ratio will strongly depend on the meteorological conditions at that time. This is avoided by turning on the source pattern for an entire month so that there is significant temporal averaging of the Green function, which helps to reduce the size of the ensemble needed to obtain meaningful climatological averages. The choice of a 1-month square pulse is convenient for two reasons. First, the state resulting from a constant source is the simple sum of the smoothed Green functions for each month and, second, the response to a 1-month pulse is essentially just the average of the δ-function-source Green function over 1 month of source time, t' (see below).

The numerical determination of the full Green function, that is, the response to a point source at every possible GCM grid point, would be a formidable task. We simplify matters by considering only surface sources with typical emission patterns such as that for SF$_6$ (Fig. 1a), which are concentrated at just a few locations, primarily in the Northern Hemisphere. Specializing to surface sources, S in (1) takes the form

$$S(p, \mathbf{x}, t) = g\delta(p - p_s)\Phi(\mathbf{x}, t), \quad (7)$$

where Φ is the (effective) surface mass flux of tracer. We consider the δ function of (7) to be just in the interior

of the atmosphere and in practice tracer is injected into the lowest model level while zero-flux boundary conditions are enforced at all times.

Formally, the smoothed, or "coarse-grained," Green function is then defined as follows. Symbolically, we replace the delta-function expansion $\Phi(\mathbf{x}, t) = \int d^2x' \, dt'\Phi(\mathbf{r}', t')\delta(\mathbf{x} - \mathbf{x}')\delta(t - t')$ with

$$\Phi(\mathbf{x}, t) = \sum_{l,m} \sigma_{l,m}\Delta_s(\mathbf{x} - \mathbf{x}_l)\Delta(t - t_m), \quad (8)$$

where $\Delta_s(\mathbf{x} - \mathbf{x}_l)$ is a localized 2D spatial surface pattern centered on position $\mathbf{x}_l$ (but reasonably smooth over several grid boxes), $\Delta(t - t_m)$ is a 1-month square pulse beginning at $t = t_m$, and $\sigma_{l,m}$ is the source strength of the pulse. Both $\Delta_s(\mathbf{x})$ and $\Delta(t)$ are normalized to unity $[\int d^2x \, \Delta_s(\mathbf{x}) = 1$ and $\int dt \, \Delta(t) = 1]$ and we may think of them as broadened δ functions. We denote the coarse-grained Green function by $G_{l,m}$, where l labels the location of the pattern center, and m labels the month during which the pattern is "turned on." Paralleling (2), $G_{l,m}$ is then defined by

$$(\partial_t + \mathcal{T})G_{l,m}(\mathbf{r}, t) = \Delta_3(\mathbf{r} - \mathbf{r}_l)\Delta(t - t_m), \quad (9)$$

with $\Delta_3(\mathbf{r} - \mathbf{r}_l) \equiv g\delta(p - p_s)\Delta_s(\mathbf{x} - \mathbf{x}_l)$. The solution for mixing ratio, χ, with a source expanded as in (8), and zero initial condition, then simply becomes the sum

$$\chi(\mathbf{r}, t) = \sum_{l,m} \sigma_{l,m}G_{l,m}(\mathbf{r}, t), \quad (10)$$

which is the coarse-grained analog of (3). Equations (9) and (10), together with the form (4) for the transport operator, are the key equations for this work. That $G_{l,m}$ is indeed a smoothed δ-function-response Green function can easily be seen by expressing it in terms of G:

$$G_{l,m}(\mathbf{r}, t) = \int d^3r' \, dt' G(\mathbf{r}, t_m | \mathbf{r}', t')\Delta_3(\mathbf{r}' - \mathbf{r}_l)$$
$$\times \Delta(t' - t_m). \quad (11)$$

c. Experimental design and definition of ensemble

We study two source locations (Fig. 1b) based on the maxima of the SF$_6$ emission pattern, one centered on Europe (EUR) and the other on eastern North America (ENA). These two source regions account for roughly half of the global SF$_6$ emissions (EUR $\sim$ 30%, ENA $\sim$ 22%). The intention is not, however, to construct the relevant part of the Green function for a particular problem, such as SF$_6$, but to choose localized source locations of general interest that serve to illustrate tropospheric transport and our methodology. Tracer emitted from the EUR and ENA sources can be expected to have quite different transport characteristics. Immediately after injection, prevailing westerlies transport EUR tracer into "continental" conditions over Asia, while ENA tracer experiences largely "oceanic" conditions over the Atlantic. Both the ENA and EUR sources are assigned the Gaussian shape $\Phi(\mathbf{x} - \mathbf{x}_l) \propto \exp[-(\zeta/\zeta_0)^2/2]$, where ζ is the geodesic distance be-
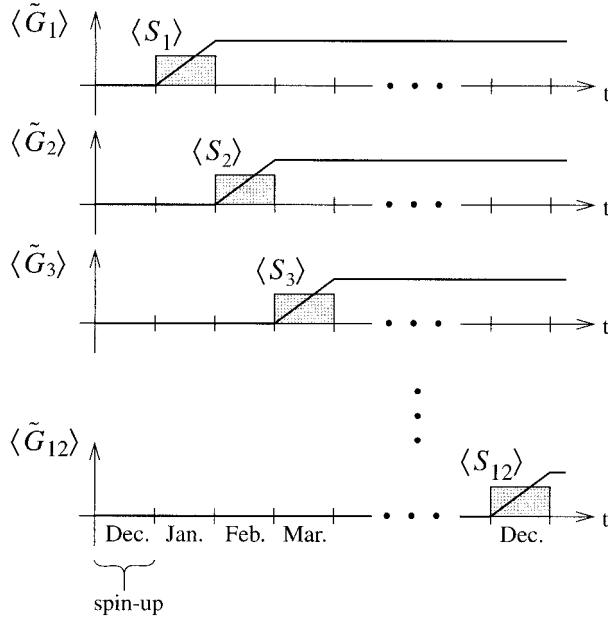
Experimental Design

FIG. 2. Experimental design as illustrated by the global integrals of the 12 Green functions vs time. The shaded functions are the corresponding source pulses.

tween $\mathbf{x}$ and $\mathbf{x}_l$, with the choice $\zeta_0 = 2\pi a/70 = 572$ km. (For this ζ_0 the area enclosed by $\zeta = \zeta_0$ includes several grid points while still being "pointlike" with ~0.2% of the global area.) The EUR pattern is centered at $\mathbf{x}_l = (50.1°N, 11.3°E)$, and the ENA pattern at $(39.0°N, 78.3°W)$.

To resolve the seasonality of the dependence of G on source time, t', the GCM was integrated with 12 tracers, $G_{l,1}, G_{l,2}, \ldots, G_{l,12}$, for each source pattern (EUR, $l = E$, and ENA, $l = A$). Tracer $G_{l,1}$ has its source turned on during January, $G_{l,2}$ during February, and so on. To ensure that the $G_{l,m}$ correspond to coarse-grained Green functions of the previous section, they are normalized such that (after the source ceases) $\int G_{l,m} d^3r = 1$. The GCM integration is started on 1 December of nominal year 1. The members of the ensemble of runs are defined through their 1 December initial conditions taken from successive years of a long multiyear run. After integrating a given ensemble member through December of year 1, the source for each $G_{l,m}$ is turned on during month m of year 2, as illustrated schematically in Fig. 2. The GCM integration is continued with all 12 tracers for several more months into year 3, until the $G_{l,m}$ no longer have any interesting spatial structure, that is, until the $G_{l,m}$ are close to G_∞. In addition, we also performed 5-yr runs with constant sources to illustrate some of the basic properties of the statistically stationary state. For all GCM runs an annual cycle of climatological sea surface temperatures was specified.

By ensemble, or climatological, average of some quantity, X, we simply mean $\{X\} \equiv \Sigma_{n=1}^{N} X_n/N$, where n labels realizations (runs). For later convenience, we estimate the variance of ensemble fluctuations, $X^\dagger \equiv X - \{X\}$, as $\{X^{\dagger 2}\}$. [This maximum likelihood estimator differs from the more usual unbiased estimator, $\Sigma_{n=1}^{N} \chi^{\dagger 2}_n/(N - 1)$, by a factor of $(N - 1)/N$.]

All diagnostic calculations were done with data saved every 6 h. Most fields were sampled every 6 h, but surface fields and subgrid terms were averaged over the 6-h period. This relatively high output rate was necessary to avoid temporal aliasing of thermal tides and the near-surface diurnal cycle. (Aliasing of tides at a 12-hourly sampling seriously contaminates the divergence of the vertically integrated tracer flux in the Tropics.) Because of the data volume generated with 12 traces for each source pattern, we content ourselves here with an ensemble of $N = 3$ members, which is sufficient for this study (see below).

Because we have adopted pressure coordinates for our diagnostics, and much of the tracer is concentrated at low levels, it is important that locations where pressure surfaces are pierced by the topography are properly handled. Therefore, all zonal and temporal averages are computed only over physical locations where $p \leq p_s$ (Boer 1982).

3. The statistically quasi-stationary state for constant sources

Much of our analysis of the Green function is motivated by a desire to understand better the statistically stationary state with constant sources. After a constant source has been applied for a long time, the mixing ratio consists of a linearly growing, spatially homogeneous background $\chi_0(t)$, plus a statistically (cyclo)-stationary part $\chi^+(\mathbf{r}, t)$. To see that χ^+ reaches a statistically stationary state, consider its equation of motion. Using $\chi = \chi_0 + \chi^+$ in (1), we have

$$\partial_t \chi^+ + \mathcal{T}(\chi^+) = S - \Sigma, \qquad (12)$$

with $\Sigma \equiv \partial_t \chi_0$. The mass-weighted global (horizontal and vertical) integral of (12) gives

$$\Sigma = \frac{\int d^3 r S(r)}{\int d^3 r} = g\langle\Phi\rangle/\langle p_s\rangle. \qquad (13)$$

(It is assumed here that the global average of the surface pressure, $\langle p_s\rangle$, is strictly time independent, as is the case for the GCM used.) Denoting the vertical integral of some quantity X by $\tilde{X} \equiv \int_0^{p_s} X\, dp/g$,

$$\tilde{S} - \tilde{\Sigma} = \Phi - p_s\langle\Phi\rangle/\langle p_s\rangle. \qquad (14)$$

Thus, $\langle \tilde{S} - \tilde{\Sigma}\rangle = 0$, so that χ^+ has no net sinks or sources. This, combined with the fact that $S - \Sigma$ has no temporal trends, ensures that χ^+ attains a statistical stationary state.
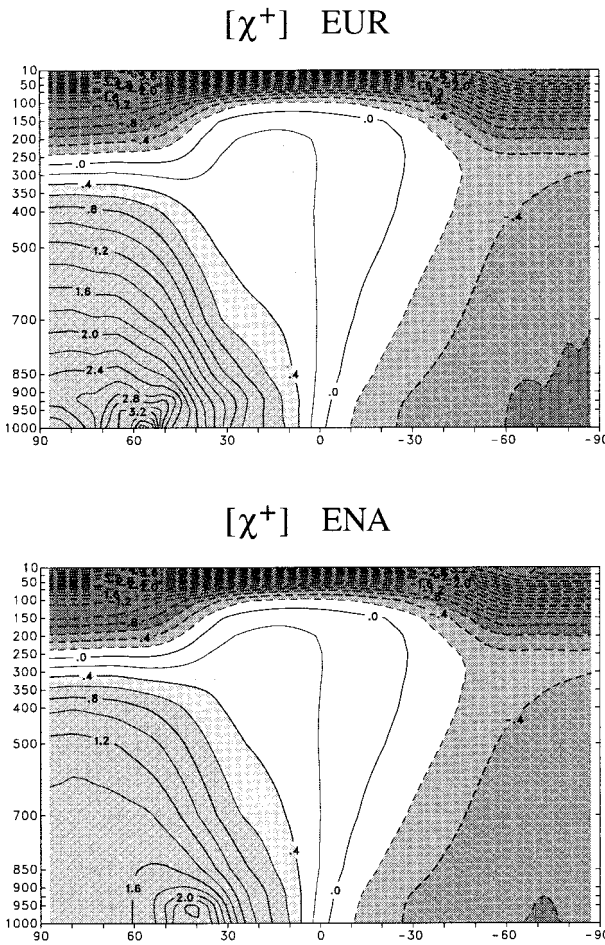
$[\chi^+]$ EUR

$[\chi^+]$ ENA

FIG. 3. Annual-mean, zonal averages of χ^+ for constant sources (EUR or ENA). The contour interval is 0.2 in units of $10\sigma G_\infty$.
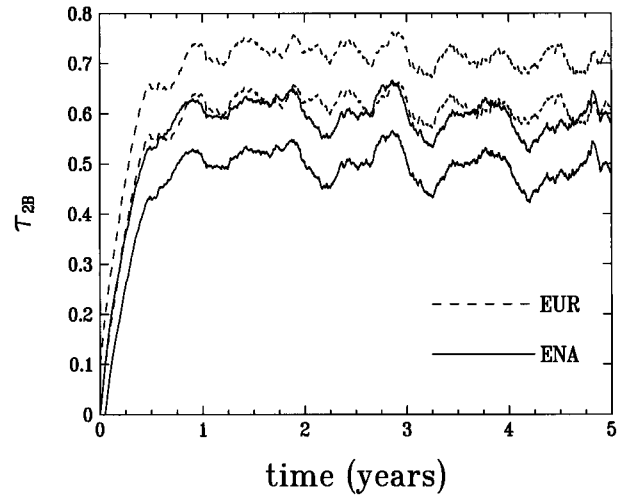

FIG. 4. Six-hourly time series of the instantaneous two-box time, τ_{2B}, in years for constant EUR source (dashed line) and ENA source (solid line). The two middle curves are the actual τ_{2B} values. The outer curves correspond to τ_{2B} shifted to disentangle the two curves for visual clarity.

The annual mean of the zonal average, $[\chi^+]$, is shown in Fig. 3 for year 5 of the simulation with constant sources. The qualitative structure of the mixing ratio in the Southern Hemisphere (SH) depends only weakly on source location. In the Northern Hemisphere (NH), the source location is identified by a maximum in mixing ratio, and the annually averaged EUR tracer tends to be "trapped" more closely to the surface than the ENA tracer. The zonally averaged structure of the mixing ratio will be discussed further when we examine it for the Green function.

A commonly used basic characterization of the statistically stationary state is the simple two-box interhemispheric exchange time, which is defined as follows (e.g., Rayner and Law 1995; Bowman and Cohen 1997). Each hemisphere represents a "box," with tracer masses M_N and M_S and sources S_N and S_S. The two-box exchange time, τ, is defined assuming a simple "downgradient" flux proportional to $\Delta M = M_N - M_S$, that is, $\partial_t M_N = -\Delta M/\tau + S_N$, and similarly for the SH. Thus, for constant sources with $\Delta S = S_N - S_S$, this two-box model exponentially approaches the steady state $2\Delta M/\Delta S = \tau$.

Paralleling the two-box model, we define an instantaneous interhemispheric exchange time as

$$\tau_{2B} \equiv 2\Delta M/\Delta S. \qquad (15)$$

Figure 4 shows the 6-hourly time series of τ_{2B} for the runs with either constant ENA or EUR source and identical realizations of the atmosphere. For these sources, an approximately statistically quasi-stationary state, with $\tau_{2B} \sim 0.6$ yr, is reached after about 1 yr. This value is within the range $0.50 \leq \tau_{2B} \leq 1.28$, with median $\tau_{2B} = 0.78$, produced by the 10 models of the TransCom2 intercomparison study (Denning et al. 1997). The small downward trend in τ_{2B} is likely due to the fact that the model's poorly represented stratosphere is still "equilibrating" with the troposphere through slow exchange. The seasonality of τ_{2B} is seen to depend on source location. For ENA, τ_{2B} has a spring trough and a fall peak, while τ_{2B} for the EUR source has a trough during spring and fall and peaks during summer and winter.

We will investigate further properties of the statistically stationary state together with the corresponding properties of the Green function. This will give us further insight into the seasonality of χ^+ and its dependence on source location.

4. Generic and modeled time evolution of G at a point

In addition to the global two-box time, it is useful to have a local measure of transport times. To this end, consider Fig. 5, which shows an idealized sketch of the generic time dependence of the ensemble-averaged G at a given field point $\mathbf{r}$. In this section, we will focus on the dependence on delay, ξ, and ignore the explicit dependence on source time, t'. Equivalently, we may
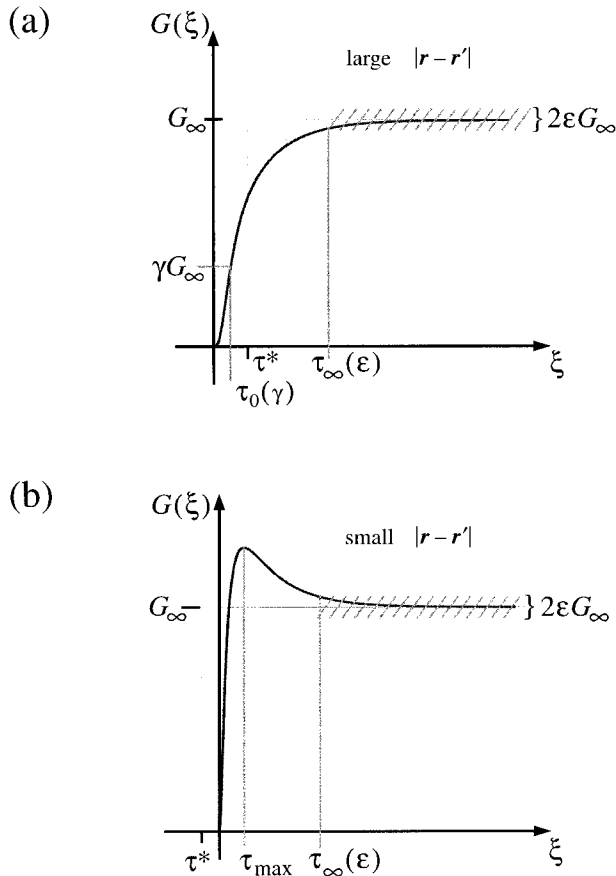
(a)

(b)

FIG. 5. (a) Sketch of the generic, smoothed, time dependence of G at a point remote from the source point. Here G asymptotically reaches its ultimate well-mixed value of G_∞ from below. (b) Generic time dependence at a point close to the source. Here G overshoots its asymptotic value and relaxes to G_∞ from above. The time τ_0 is the time when G first reaches γG_∞, while the time $\tau_\infty(\epsilon)$ is the time such that for all later times $|G - G_\infty| < \epsilon G_\infty$. The time τ^* is the integral time defined such that the area under the curve is equal to that of the shaded region as $\xi \to \infty$ (see appendix).

imagine dealing with an annual average over t'. (The dependence on t' can explicitly be dealt with, but would unnecessarily encumber the discussion here.) If $\mathbf{r}$ is far from the source point $\mathbf{r}'$ (Fig. 5a), the mixing ratio at $\mathbf{r}$ monotonically increases to its eventual asymptotic value, G_∞. For field points $\mathbf{r}$ close to the source (Fig. 5b), one expects an overshoot as very high mixing ratios are observed shortly after injection followed by a relaxation to G_∞ from above. Oscillations about G_∞ for intermediate times are in principle also possible as an air mass with high mixing ratio recirculates to $\mathbf{r}$ before having been significantly diluted, but we expect such behavior to be associated with short time and length scales and, therefore, to be largely averaged out for the ensemble mean of the coarse-grained G.

What is the evolution of $G(\xi)$ as a function of ξ at a point in the GCMs atmosphere? Clearly we cannot plot $G(\xi)$ versus ξ for every model grid point. Instead, we

parameterize the form of $G(\xi)$ in terms of a few constants. First, does $G(\xi)$ overshoot its asymptotic value, G_∞? As a direct measure of whether this occurs, we define an overshoot measure, α. If G_{max} is the peak value of $G(\xi)$, then $\alpha = 1$ if $G_{max} > G_\infty$, and $\alpha = 0$ otherwise. Correspondingly, we define τ_{max} as the delay time for which G reaches G_{max}. It is natural to ask how long it takes for G to first reach some specified value. We define $\tau_0(\gamma)$ to be the time when G first reaches γG_∞. Thus, with $\gamma = \frac{1}{2}$, τ_0 has a natural interpretation as arrival time. Finally, one can also ask how long it takes for $G(\xi)$ to be within a specified range of G_∞, as a crude measure of the time when $G(\xi)$ is "asymptotic." Accordingly, we define $\tau_\infty(\epsilon)$ as the time when $|G/G_\infty - 1| \le \epsilon$ for all delays $\xi \ge \tau_\infty$. We thus have four "shape" parameters for the $G(\xi)$ versus ξ curve: the timescales τ_{max}, τ_0, and τ_∞, plus the overshoot measure α.

To determine the spatial structure of these parameters, we compute them at each point in the atmosphere by linearly interpolating 19 consecutive monthly means of the ensemble-averaged G. To compute a meaningful overshoot measure, α, we consider the following: after 19 months, G is homogenized to withing a few percent throughout the troposphere but still exceeds G_∞ by ~6% because G has not yet been mixed throughout the stratosphere. In this sense, G strictly overshoots G_∞ everywhere in the troposphere. However, we wish to compute an α that indicates whether G overshoots its tropospheric mixed state, and therefore in practice demand that G_{max} exceed G_∞ by about 6% for α to be set to unity. (The qualitative features of α do not depend strongly on where this threshold is set.)

Figure 6 shows the zonal averages of these parameters for $G_{E,1}$. Even in the zonal average, the boundary between $[\alpha] = 0$ and $[\alpha] = 1$ is surprisingly sharp, and consists of the tropopause in the NH and of a less obvious boundary in the SH, which cannot be identified as a transport barrier. The fields $[\tau_{max}]$ and $[\alpha]$ contain similar information. For much of the region, where G does not overshoot its tropospheric mixed value, G_{max} is the latest value in the time series (i.e., $\tau_{max} \simeq 18$ months), consistent with a monotonic approach to the tropospheric mixed value from below. As one gets closer to the source, τ_{max} decreases continuously, since there G_{max} represents the advecting and diffusing initial tracer pulse shortly after injection. The arrival time $\tau_0(\frac{1}{2})$ shows that where G overshoots ($[\alpha] = 1$), it reaches $G_\infty/2$ in a time on the order of $\tau_{max}/2$, while, where $[\alpha] = 0$, $\tau_{1/2}$ contains structure not captured by τ_{max}. Finally, τ_∞ shows when G has asymptoted to within 10% of G_∞ (either from above or below). [At $\epsilon = 10\%$, $\tau_\infty(\epsilon)$ is not sensitive as to whether we take the asymptotic value of G to be G_∞ or the tropospheric mixed value at 19 months.] The minimum values of τ_∞ lie along the boundary of the overshoot region as expected from a continuous transition from one behavior to the other. What this means physically is less clear, though presumably balanced fluxes are necessary so that a value of G_∞ is

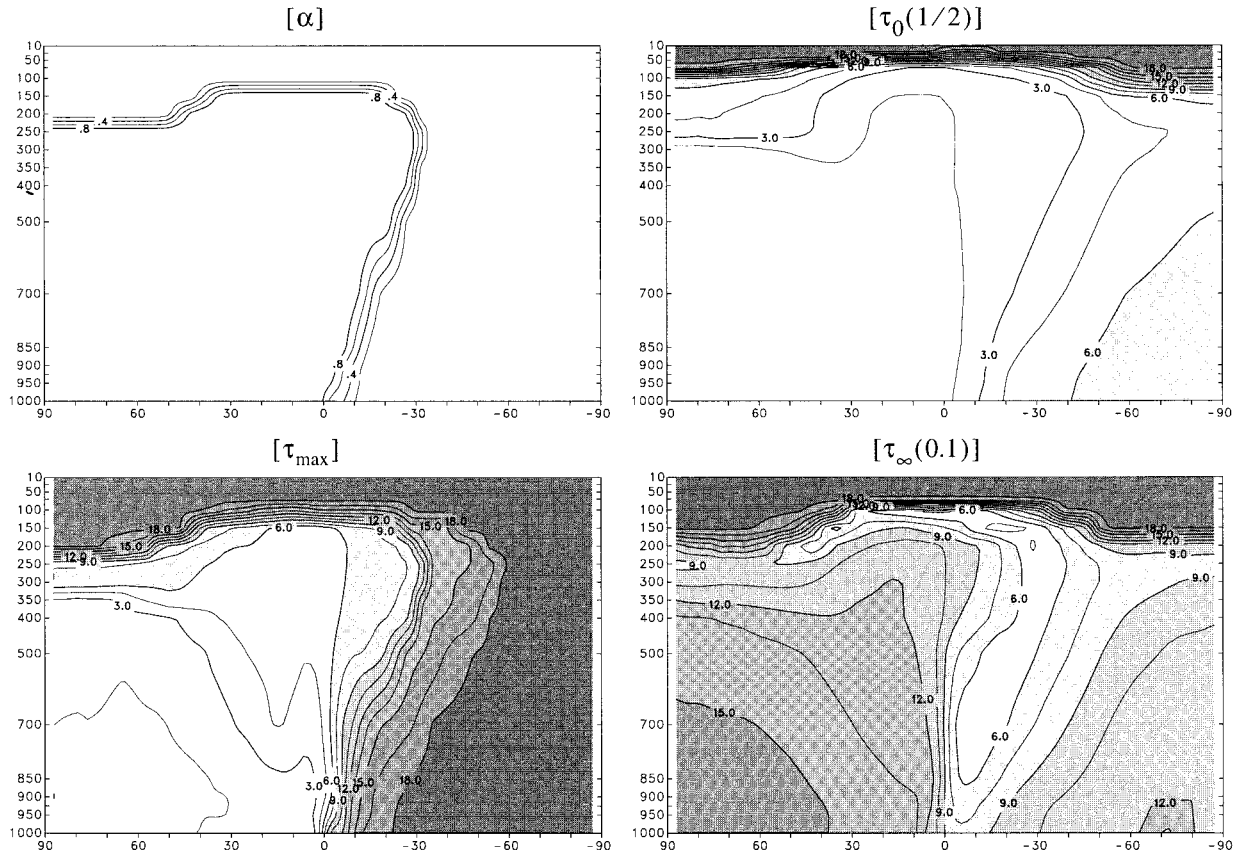## Characterization of the time evolution of G_1 (EUR)

FIG. 6. Zonal average of the overshoot measure, α, (contour interval of 0.2) and the three timescales (contour interval of 1.5 months) that parameterize the time evolution of G at a point as described in the text (see also Fig. 5).

quickly established without further net loss or gain of tracer mass. (All timescales are largest above the tropopause across which tracer leaks slowly with a timescale on the order of a decade for this model.)

One can also define an integral time, τ^*, such that the area under the $G(\xi)$ versus ξ curve, for $\xi \leq t$, approaches $(t - \tau^*)G_\infty$ for large t. For $\tau^* \gg 0$, τ^* has a natural interpretation as an arrival time much like $\tau_0(\frac{1}{2})$. The virtue of τ^* is that the mixing ratio of the statistically stationary state for constant sources can simply be scaled to equal τ^* in the case of a point source, or to a weighted average of τ^* for a distributed source. These properties of τ^* are derived in the appendix.

While the timescales associated with the relaxation of G to G_∞ at a point in the atmosphere are a useful characterization of transport, they do not carry explicit information on transport pathways. Extracting transport pathways directly from the statistically stationary state is nearly impossible, but this kind of information is exactly what is naturally contained in G and this will be the subject of the following section.

5. Basic structure and seasonality of the climatological Green function

We consider the ensemble and monthly averaged Green functions $G_{l,m}$ for the EUR and ENA sources. (For clarity, we omit the { ... } brackets for ensemble average, so that an overbar indicates the combined monthly and ensemble average.) As a basic characterization of the horizontal spatial structure of G and its transport, we compute the vertical integral $\tilde{G} \equiv \int_0^{p_s} G \, dp/g$ (the "column burden" per mass injected), which obeys from (9)

$$\partial_t \tilde{G}_{l,m} + \boldsymbol{\nabla} \cdot (\widetilde{\mathbf{v}G}_{l,m}) = \tilde{\mathcal{D}}_H + \Delta_s(\mathbf{x} - \mathbf{x}_l)\Delta(t - t_m). \quad (16)$$

After the source pulse has ceased [$\Delta(t - t_m) = 0$], the right-hand side (rhs) of (16) is just $\tilde{\mathcal{D}}_H$, which is small compared with the remaining terms. It is useful to split the vertically integrated flux $\widetilde{\mathbf{v}G} \equiv \mathbf{G}$ into its rotational and divergent parts as $\mathbf{G} = \mathbf{G}_D + \mathbf{G}_R = \boldsymbol{\nabla}\Pi + \mathbf{k} \times \boldsymbol{\nabla}\Psi$, with potential and streamfunctions Π and Ψ. Because $\boldsymbol{\nabla} \cdot \mathbf{G} = \boldsymbol{\nabla} \cdot \mathbf{G}_D = \nabla^2\Pi$, only the divergent part, $\mathbf{G}_D$, contributes to (16). Figures 7a,b show the ensemble

and monthly averages of $\tilde{G}_1$ and $\tilde{G}_7$, together with their associated $\mathbf{G}_D$, for the source month (January and July) and for the subsequent 2 months. Note that $\overline{\mathbf{G}}_D$ is a purely diagnostic quantity and after $\sim$1 month $\overline{\mathbf{G}}_D$ is at least an order of magnitude smaller than $\overline{\mathbf{G}}_R$ (as $\xi \rightarrow \infty$, $\overline{\mathbf{G}}_D \rightarrow \sim 0$, and $\overline{\mathbf{G}}_R \rightarrow \sim G_\infty \overline{\mathbf{v}}$). Also, because $\nabla \cdot \mathbf{G}_D = \nabla^2 \Pi$, $\mathbf{G}_D$ has global-scale structure even for highly localized flux divergence. For example, the structure seen in the SH at a lag of 1 month in Fig. 7 does not imply a significant net flux in the SH; virtually the same $\mathbf{G}_D$ is obtained if $\mathbf{G}$ is zeroed in the SH. The utility of $\overline{\mathbf{G}}_D$ lies in the fact that it gives a useful indication of the average spreading of tracer, and that it is the only part of $\mathbf{G}$ that enters (16).

For both source locations and all source times, tracer is mixed and transported rapidly in the zonal direction for the first 2–3 months. During this time $\tilde{G}$ has pronounced geographic dependence, and $\overline{\mathbf{G}}_D$ has a strong zonal component. After about 3 months, $\tilde{G}$ has lost most of its zonal structure and $\overline{\mathbf{G}}_D$ is primarily meridional. The evolution of $\tilde{G}$ depends on season (i.e., source time, t') and on source location. In the EUR case during winter, $G_{E,1}$ spreads primarily from west to east at early times (order 1 month) and first finds its way to the equator by ''swirling'' (with anticyclonic curvature) around the Tibetan Plateau. In contrast to this wintertime behavior, the EUR summer pulse, $G_{E,7}$, shows slower zonal mixing and tracer first reaches the Tropics over Africa and the tropical Atlantic. Summer burdens over the Himalayas are somewhat higher than in winter, indicating that the transport occurs at higher levels during summer. In the ENA case, there is less seasonal dependence on source time for the early transport. In spite of marked differences between the burdens for the two sources during the first 2 months, their similarity is striking after only 3 months, when the zonal structure has been largely homogenized.

The meridional spreading of the ''burden,'' $\tilde{G}$, is shown in Fig. 8 as a space–time plot of the zonal average $[\tilde{G}]$, sampled every 6 h. The burden is plotted as $[\tilde{G}]/\langle \tilde{G}_\infty \rangle$, so that the large-lag limit of $[\tilde{G}_\infty]$ shows as $[p_s]/\langle p_s \rangle \cong 1$. The figure shows the vertically integrated version of the generic behavior sketched for $G(\xi)$ in Fig. 5: in the NH, $[\tilde{G}]$ overshoots its asymptotic value of $[\tilde{G}_\infty]$ by a factor of $\sim$4, while in the SH $[\tilde{G}_\infty]$ is gradually approached from below. After $\sim$90 days, there is little difference between the EUR and ENA cases. The high wintertime burdens for the EUR source are in part geometric in origin: a unit mass residing at high latitudes will result in higher zonal-average burdens than the same mass at lower latitudes (and since the mixing is primarily zonal, this also means higher local mixing ratios at high latitudes). Tracer from the EUR source is efficiently transported northward in winter resulting in high burdens. Less mass reaches high latitudes from the ENA source.

A crucial aspect of tracer transport is the vertical structure of G. Figures 9a,b show $[\overline{G}]$, the zonal and

monthly/ensemble average of G together with its zonally averaged flux, $\mathbf{F} \equiv ([\overline{vG}], [\overline{\omega G}])$, due to the model's resolved advection. [The vertical component of $\mathbf{F}$ is scaled by the negative aspect ratio of the figure ($\omega > 0$ is downward). Applying this scaling, for example, to $([\overline{v}], [\overline{\omega}])$, gives vectors properly tangent to the mass streamfunction.] Not all of $\mathbf{F}$ contributes to the local rate of change of G since much of the flux is rotational in the $\phi - p$ plane. In particular, as $G \rightarrow G_\infty$, $\mathbf{F} \rightarrow ([\overline{v}], [\overline{\omega}]) \, G_\infty$, so that $\mathbf{F}$ becomes purely rotational. Nevertheless, at early times $\mathbf{F}$ does give a useful indication of the advective transport. The model's parameterized vertical flux ($-\int_0^p \mathcal{D}_V \, dp'$), discussed separately below, is also important during the source month, but adding it to $\mathbf{F}$ does not alter the qualitative character of Fig. 9.

The general structure of $[\overline{G}]$ and its evolution are in broad qualitative agreement with the picture of the zonally averaged transport given by Plumb and Mahlman (1987). The large low-level horizontal gradients in the Tropics result from the strain of the convergence of the Hadley circulation. This convergence can be seen to extrude tracer at low levels and to inject it into the upper troposphere where it enters the SH in the outflow region of the Hadley circulation. After $\sim$3 months, $[\overline{G}]$ is established in the SH with larger mixing ratios at high levels than at low levels, giving the hemispheres opposite vertical mixing ratio gradients in the zonal average. After $\sim$4 months, $[\overline{G}]$ has reached a tropospheric ''slope equilibrium'' in the sense that contours of $[\overline{G}]$ continue to have approximately the same shape (i.e., the same local slopes), while the gradients of $[\overline{G}]$ continue to get washed out as $G \rightarrow G_\infty$ (see also Fig. 15). This ''equilibrium'' state can be ascribed to an approximate local balance between the zonal-mean advection and effective eddy diffusion (Plumb and Ko 1992, and references therein).

To augment $[\overline{G}]$ with information on the vertical structure as a function of longitude, Fig. 10 shows equatorial east–west sections of $\overline{G}$ for the month following the source month. While the vertical structure of a an east–west section is sensitive to its location with respect to the intertropical convergence zone, the longitudinal structure is not. In winter, for both source cases, the equatorial cross sections show tracer entering the SH at longitudes remote from the source and at low levels. (Subsequently, at $\sim$10°S, tracer does get injected into upper troposphere by the Hadley convergence as shown in Fig. 9.) In summer, tracer is mixed more rapidly in the vertical throughout the NH and crosses into the SH closer to the longitude of the source than in winter.

From the fields presented, from animations, and numerous visualizations of the 3D evolving $G_{l,m}$, we have the following general picture. EUR tracer shows behavior we might expect for continental conditions. In winter, tracer is advected over the Asian continent where there is subsidence resulting in high mixing ratios close to the surface for about 2 months. In summer, the heating
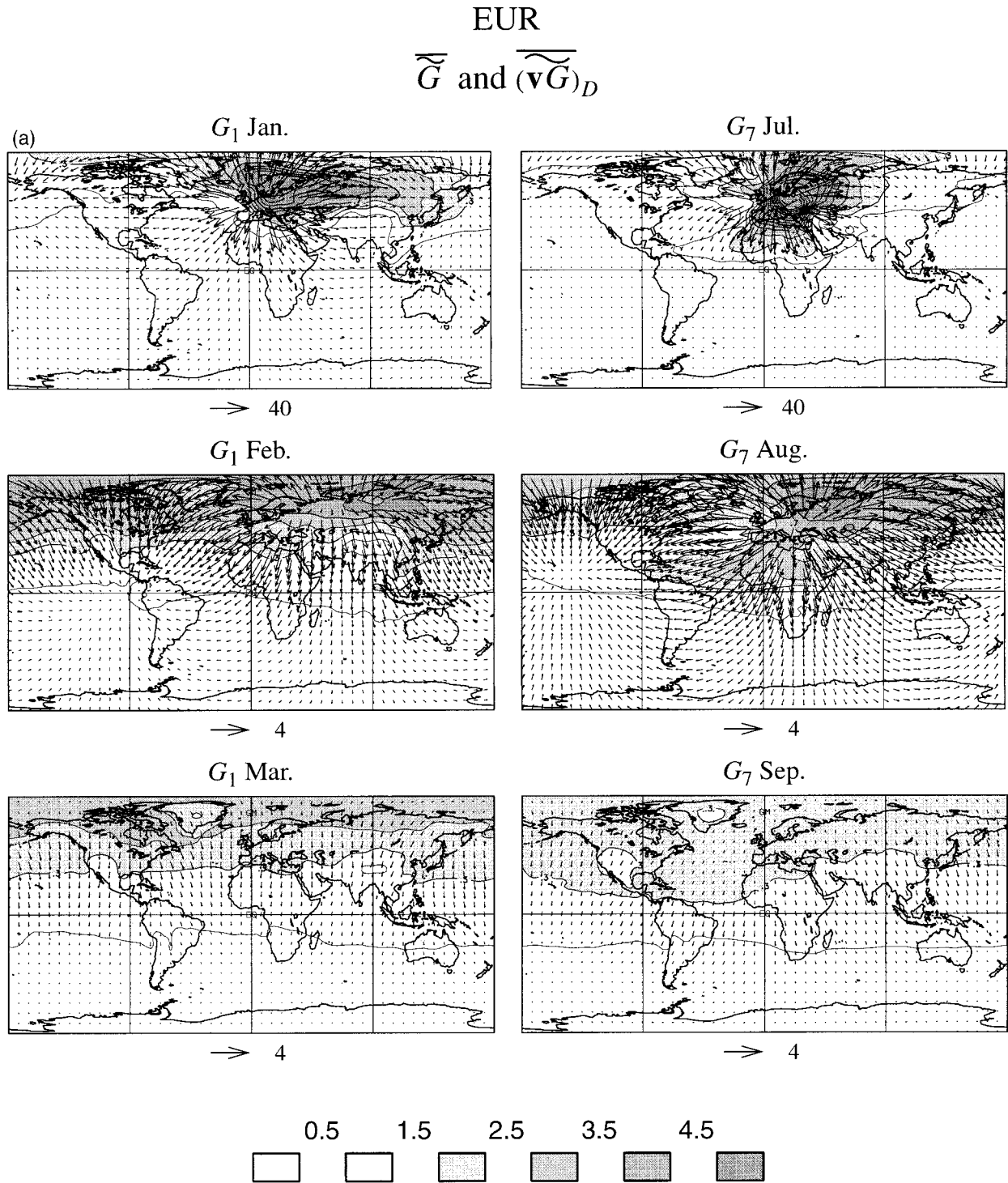
EUR

$$\overline{\tilde{G}} \text{ and } \overline{(\mathbf{v}\tilde{G})}_D$$

FIG. 7. (a) EUR source for Jan (G_1) and Jul (G_7) releases. The contoured and shaded field is the monthly and ensemble average of the vertically integrated Green function, $\tilde{G}$ in units of $\langle \tilde{G}_\infty \rangle$, and the vector field is the corresponding monthly mean divergent flux in units

over land is associated with upward motion and convection. The evolution of ENA tracer is consistent with oceanic conditions. Tracer is advected over the Atlantic and experiences vertical transport even in winter with

less of a seasonal contrast. The low-level, wintertime swirling of EUR tracer around the Tibetean Plateau, already noted, also applies to a lesser degree to the ENA case where high mixing ratios also appear off East Af-
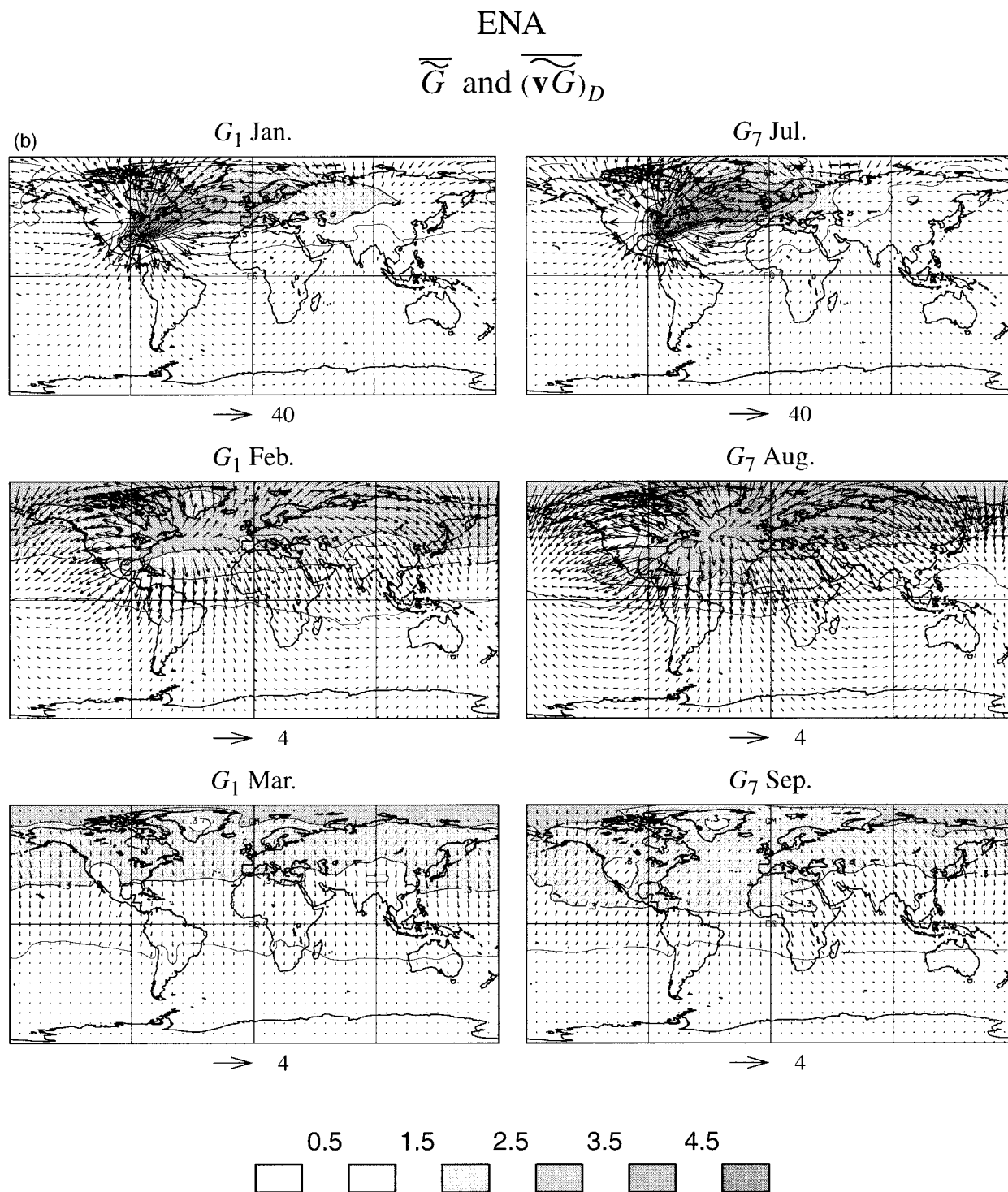
ENA

$$\overline{\widetilde{G}} \text{ and } \overline{\widetilde{(\mathbf{v}\widetilde{G})}}_D$$

(b)

G_1 Jan.

G_7 Jul.

$\longrightarrow$ 40

$\longrightarrow$ 40

G_1 Feb.

G_7 Aug.

$\longrightarrow$ 4

$\longrightarrow$ 4

G_1 Mar.

G_7 Sep.

$\longrightarrow$ 4

$\longrightarrow$ 4

0.5   1.5   2.5   3.5   4.5

FIG. 7. (*Continued*) of $\langle \tilde{G}_\infty \rangle$ m s^{-1}. Note that during the source months the scale of the vector field is an order of magnitude larger than for the other months. (b) Same as (a) for the ENA source.

rica (Figs. 7 and 10). For both source cases, there is in addition some low-level wintertime transport across the tropical Atlantic associated with the trade winds. This can be seen in Fig. 10 by the high mixing ratios off the east coast of South America for EUR and to a lesser degree for ENA. Summertime transport is more active throughout the troposphere. The dominant summer transport pathway for EUR is over western Africa and
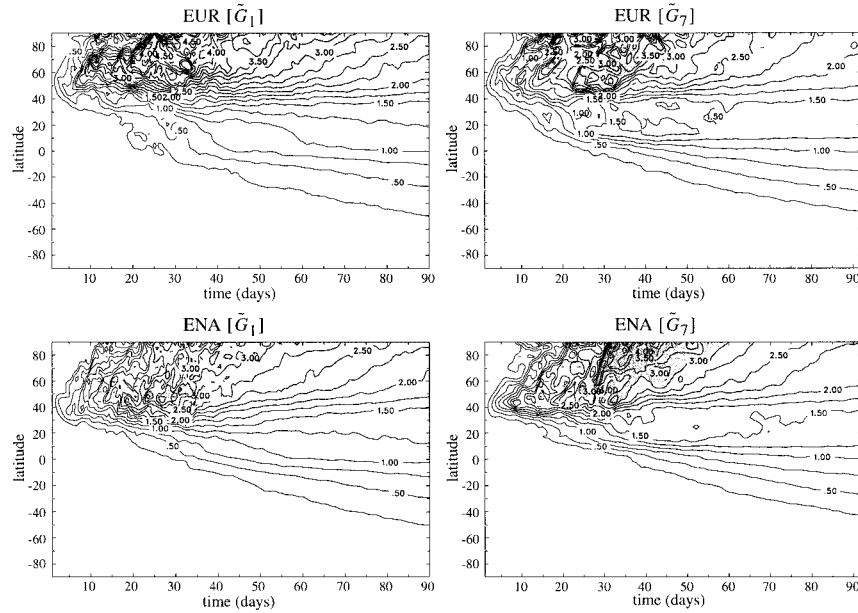
FIG. 8. The zonal average of the 6-hourly sampled, vertically integrated ensemble-mean Green function as a function of time. The contour interval is 0.25 in units of $\langle \tilde{G}_\infty \rangle$.

westward over the Atlantic at midlevels. Summertime transport of ENA tracer is dominated by northeast transport to Europe via the westerlies and southwest transport across Mexico and over the tropical Pacific.

We have seen an indication of the seasonality of G with respect to source time, t', from the contrast between January and July pulses. The seasonality of G has also been studied systematically by examining the seasonal cycle of $\overline{G}(\xi, t')$ with respect to t', at fixed lag ξ, in accord with (6). For example, for a fixed lag of 1 month we examined the annual cycle of the 12 monthly means corresponding to the February average of the January pulse, the March average of the February pulse, and so on, for the ensemble-averaged 12 $G_{l,m}$. [We define the annual cycle here simply as the gravest mode ($n = \pm 1$) of the Fourier expansion (6).] For the fields $\tilde{G}$, $[G]$, and the east–west sections of G, this analysis shows that the character of the seasonal dependence on t' is well captured by the contrast between the January and July pulses presented. With increasing lag, the seasonal cycle amplitude, as well as the differences between the EUR and ENA cases, decrease.

From a modeling perspective it is of considerable interest to establish the relative importance of resolved versus parameterized vertical transport. For this purpose we write the monthly (and ensemble) averaged equation of G as

$$\overline{\partial_t G} + \overline{\mathbf{v}} \cdot \nabla \overline{G} + \nabla \cdot \overline{\mathbf{v}' G'} + \overline{\omega} \partial_p \overline{G} + \partial_p \overline{\omega' G'}$$

$$= \overline{\mathcal{D}}_H + \overline{\mathcal{D}}_V, \qquad (17)$$

using (9) and (4), with the definition $X \equiv \overline{X} + X'$ for some quantity X. (During the source month, there is an additional source term on the rhs.) As suggested by this form of the equation, we compare the so-called tendency due to parameterized vertical transport, $\overline{\mathcal{D}}_V$, with the tendency due to resolved vertical transport, $\overline{\mathcal{T}}_V \equiv -(\overline{\omega} \partial_p \overline{G} + \partial_p \overline{\omega' G'})$. Both $\overline{\mathcal{D}}_V \rightarrow 0$ and $\overline{\mathcal{T}}_V \rightarrow 0$ as $G \rightarrow G_\infty$, as must be the case for any reasonable measure of transport tendency. Since $\mathcal{D}_V$ vanishes on vertical integration, we compute as a global measure of the overall strength of the two terms the global (horizontal and vertical) integrals of their absolute values. As a measure of the relative strengths of the two terms, we form the ratio $R \equiv \langle \int dp |\overline{\mathcal{D}}_V| \rangle / \langle \int dp |\overline{\mathcal{T}}_V| \rangle$. Figure 11 shows R as a function of lag time for G_1 and G_7. Although at very early times, when tracer resides primarily in the boundary layer, parameterized transport must dominate, Fig. 11 shows that even for tendencies averaged over the source month, R barely exceeds unity and in one case (G_1, EUR) $\overline{\mathcal{T}}_V$ already dominates. With increasing lag $\overline{\mathcal{D}}_V$ and $\overline{\mathcal{T}}_V$ decay to zero, but after ~3 months R decreases only very slowly with $R \sim \frac{1}{3}$ after 6 months. Note that at early times R is largest for the summer-release cases, as might be expected from more vigorous midlatitude summertime convection. The inset of Fig. 11 shows R for year 5 of the run with constant sources. In the quasi-stationary state $R \sim 0.4$ with a more pronounced seasonal cycle for the EUR case.

The tendencies $\overline{\mathcal{T}}_V$ and $\overline{\mathcal{D}}_V$ are of course not equally important everywhere. To give an indication of their spatial distribution, we show in Fig. 12 their zonal averages for the month following the source month, averaged over all 12 $G_{l,m}$. The parameterized transport, $\overline{\mathcal{D}}_V$, is largest close to the surface, where it removes

tracer from the boundary layer and the resolved transport is relatively weak. The resolved transport tendency near the surface is dominated by the eddy component $-\partial_p \overline{\omega' G'}$ (not shown separately). The large implied downward flux seen for the EUR case at ~35°N is associated with eddy transport in the oceanic storm tracks. For $p \gtrsim 500$ mb, $\overline{\mathcal{D}}_V$ does contain some representation of deep convection, but $\overline{\mathcal{T}}_V$ is approximately five times larger. The simple layer-by-layer convective adjustment scheme used is necessarily less efficient at transporting tracer to the upper troposphere than a penetrative cumulus convection scheme.

6. Structure and seasonality of eddy transport

The monthly mean circulation plays an important role in transport, but eddies are equally important. We will first discuss the eddy transport for the statistically stationary state and then examine how these stationary-state eddies are synthesized from their time-lagged counterparts of the Green function. The standard eddy decomposition of a variable X in statistically stationary state is $X = [\overline{X}] + \overline{X}^* + X'$, where $X' \equiv X - \overline{X}$ are the "transient" eddies, and $\overline{X}^* \equiv \overline{X} - [\overline{X}]$ are the "standing" eddies. (As before, the overbar is a combined monthly and ensemble average and the brackets, $[\ldots]$, denote a zonal average.)

The zonally and monthly/ensemble-averaged tracer equation (1) reads

$$\overline{\partial_t[\chi]} + \partial_y[\overline{v\chi}] + \partial_p[\overline{\omega\chi}] = [\overline{S}] + [\overline{\mathcal{D}}], \quad (18)$$

where $\partial_y X \equiv (a\cos(\phi))^{-1} \partial_\phi(\cos\phi X_\phi)$, and $\mathcal{D} \equiv \mathcal{D}_V + \mathcal{D}_H$. The statistically stationary flux $[\overline{v\chi}]$ can be partitioned into its mean-motion, standing-eddy, and transient-eddy components:

$$[\overline{v\chi}] = [\overline{v}][\overline{\chi}] + [\overline{v}^*\overline{\chi}^*] + [\overline{v'\chi'}], \quad (19)$$

and similarly for $[\overline{\omega\chi}]$. Whether or not the background mixing ratio, χ_0, is subracted from $\chi = \chi^+ + \chi_0$ [cf. Eq. (12)] makes a negligible difference for the eddy terms since $\overline{\chi}_0^* \equiv 0$, and $[\overline{v'\chi_0'}] = 0$ to an excellent approximation. We will consider the mean-motion term only vertically integrated, so that again it does not matter if χ_0 is removed since $[\overline{v}] = 0$ to an excellent approximation.

The net meridional flux accomplished by each transport term is given by its vertical integral. In the statistically stationary state $\overline{\partial_t[\chi^+]}$ and $[\overline{\mathcal{D}}_H]$ are small so that, with $\overline{\partial_t[\chi]} = \overline{\partial_t \chi_0} \equiv \Sigma$ and $p_s/\langle p_s \rangle \cong 1$, the vertical integral of (18) gives the first-order balance

$$\partial_y[\widetilde{\overline{v\chi}}] \cong [\Phi - \langle \Phi \rangle]. \quad (20)$$

Equation (20) shows that $[\widetilde{\overline{v\chi}}]$ contains little more information than what source has been specified. The interest here lies, therefore, in the nature of the partition of the essentially constrained flux, $[\widetilde{\overline{v\chi}}]$, into $[\widetilde{\overline{v}][\overline{\chi}}]$, $[\widetilde{\overline{v}^*\overline{\chi}^*}]$, and $[\widetilde{\overline{v'\chi'}}]$. Figure 13 shows space–time plots of these three components, together with $[\widetilde{\overline{v\chi}}]$, for

year 5 of the simulation with constant sources. The weak seasonality of $[\widetilde{\overline{v\chi}}]$ shows the degree to which $\overline{\partial_t[\widetilde{\chi^+}]}$ can be neglected in (20). The fluxes are largest in the vicinity of the source, which maintains high gradients. All three components are of the same order of magnitude, and no single mechanism, in this diagnostic sense, dominates in the NH. The mean-motion and standing-eddy terms show a strong seasonality consistent with the seasonal movement of the Hadley cell and the monsoon. The southward flow between the equator and ~30°N, associated with the lower branch of the Hadley cell during winter, weakens to the point of weak reversal during summer. Since the total transport is approximately constrained to be time independent by (20), the eddy transport takes over when $[\overline{v}][\overline{\chi}]$ slackens. Presumably because of the large standing structures associated with the monsoon, the standing eddies take over the bulk of the transport from the mean motion, while the tropical transient eddies show relatively little seasonality. In the SH, transient-eddy transport dominates for two reasons. The mixing ratio is largely zonally symmetric in the SH so that $[\overline{v}^*\overline{\chi}^*]$ is small, and the mixing ratio has weaker vertical gradients in the SH (see Fig. 9) giving a weaker mean-motion term (if $[\overline{\chi}]$ had no vertical structure, $[\overline{v}][\overline{\chi}] = [\overline{\chi}][\widetilde{\overline{v}}] = 0$). There is considerable difference in the seasonality of the eddies between the two source cases. The standing eddies are weaker for ENA tracer consistent with the fact that the ENA Green function is more homogenized by the time it reaches the monsoon region than is the case for EUR tracer.

We now ask how much Green function $G_{l,m}$ contributes to the mean-motion and eddy fluxes of the statistically stationary state. From (10) it follows that the eddy fluxes of χ for month m can be written as a sum of the corresponding lagged eddy fluxes (or "eddy contributions") of the G's. Thus, for the transient eddies we have

$$[\overline{v'\chi'}] = \sigma \sum_{n=0}^{\infty} [\overline{v'G'_{m-n}}], \quad (21)$$

with similar expressions for the standing-eddy and mean-motion terms and their vertical counterparts. [In (21) we assumed for definiteness a single source pattern of constant strength σ.] Since G itself is never in statistically stationary state, the deviations $\overline{G}^*$ cannot be considered to be truly "standing" eddies. Similarly, $[\overline{G}]$ and G' do not carry quite the same interpretations as in the statistically stationary case. However, even in the case of a constant source, χ^+, and indeed any other climate variable, is only *cyclo*-stationary, and as we have just seen, the standing eddies do change from month to month. After their source pulse has ceased, the $G_{l,m}$ do not change significantly more rapidly than χ^+ so that one can, at least to a first approximation, think of the eddy terms of (21) in much the same way as one would in the statistically stationary case. It is certainly legitimate and interesting to examine the terms

EUR

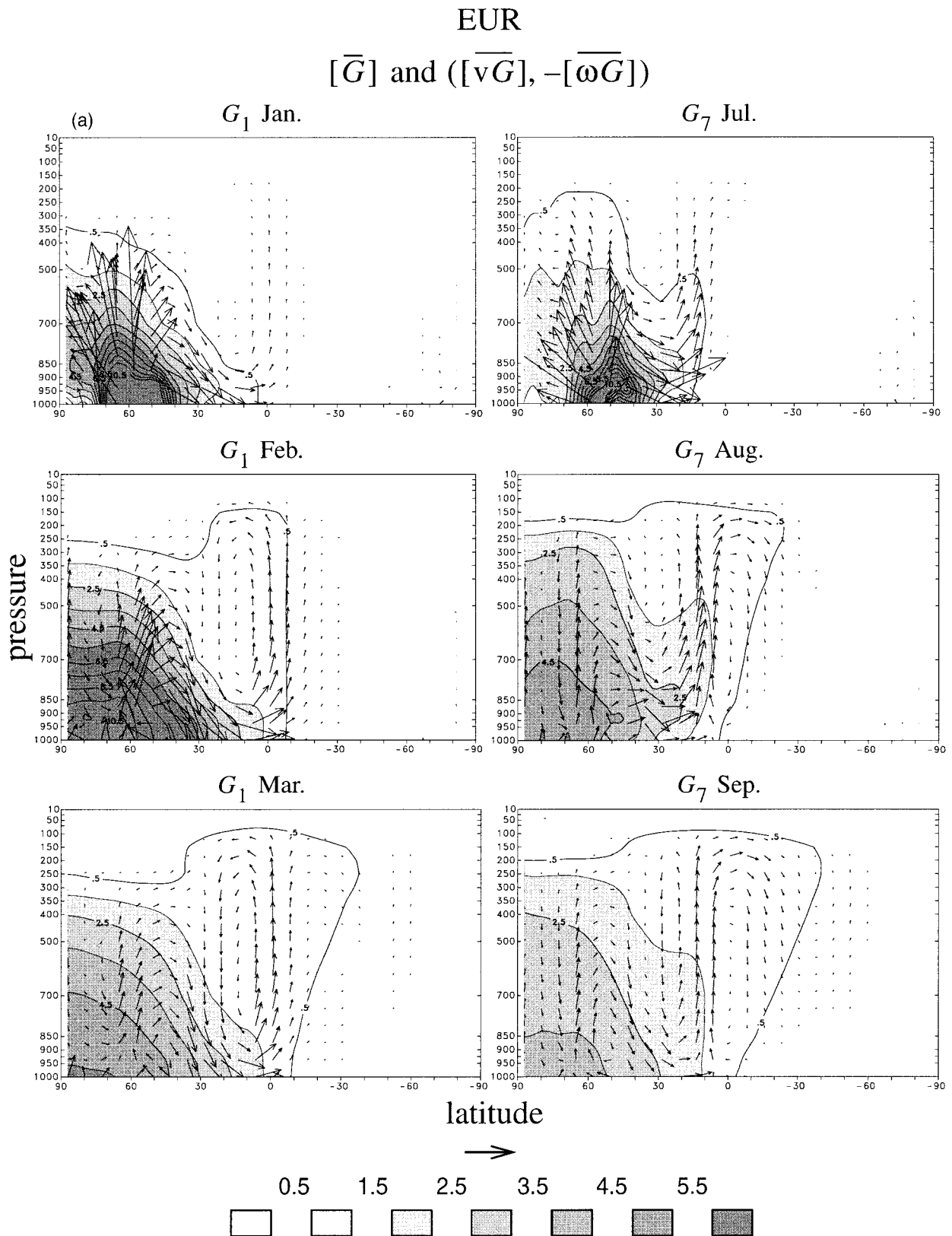$$[\bar{G}] \text{ and } ([\overline{vG}], -[\overline{\omega G}])$$

FIG. 9. (a) EUR source. The ensemble, monthly, and zonally averaged Green function and its resolved flux (vectors) for the release times (subscripts) and months indicated. The contour interval is 1.0, with the lowest contour at 0.5 and the highest contour at 10.5, in units of G_∞.

ENA

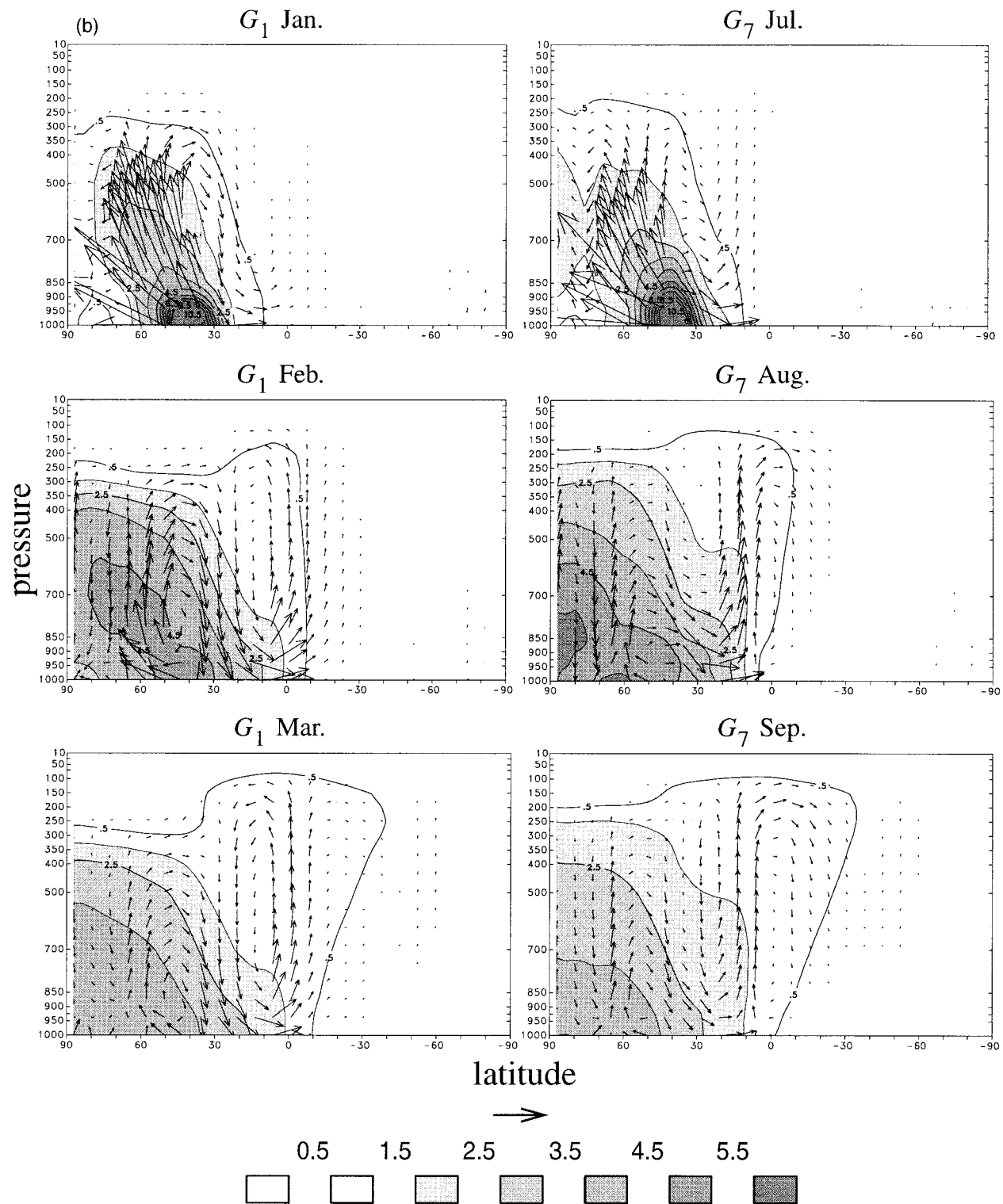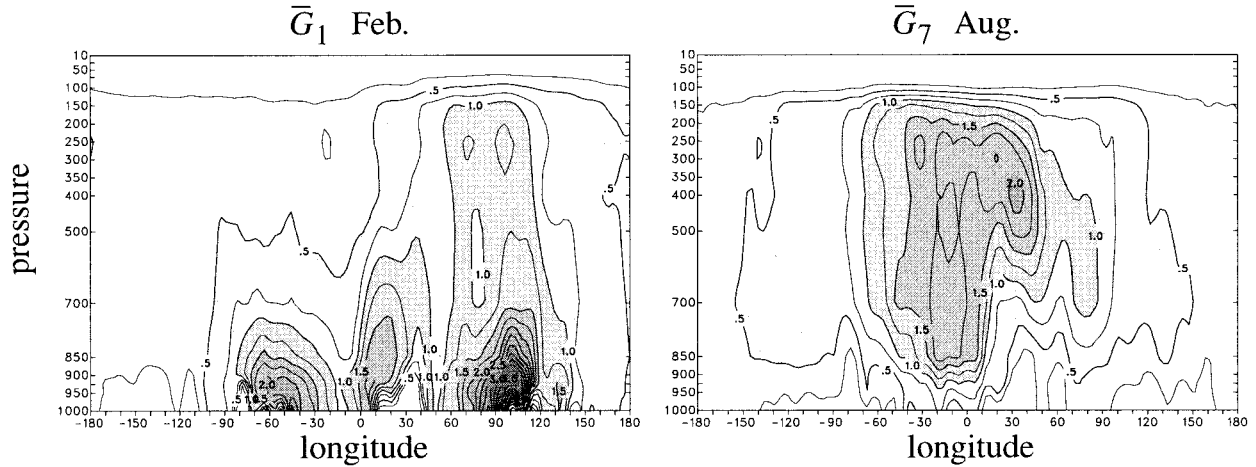$$[\overline{G}] \text{ and } ([\overline{vG}], -[\overline{\omega G}])$$

FIG. 9. (*Continued*) The vector scale indicates a horizontal flux $10G_\infty$ m s^{-1}. The vertical components of the fluxes have been scaled as described in the text. (b) Same as (a) but for the ENA source.

equatorial sections of G

EUR

$\overline{G}_1$ Feb. $\overline{G}_7$ Aug.

ENA

$\overline{G}_1$ Feb. $\overline{G}_7$ Aug.
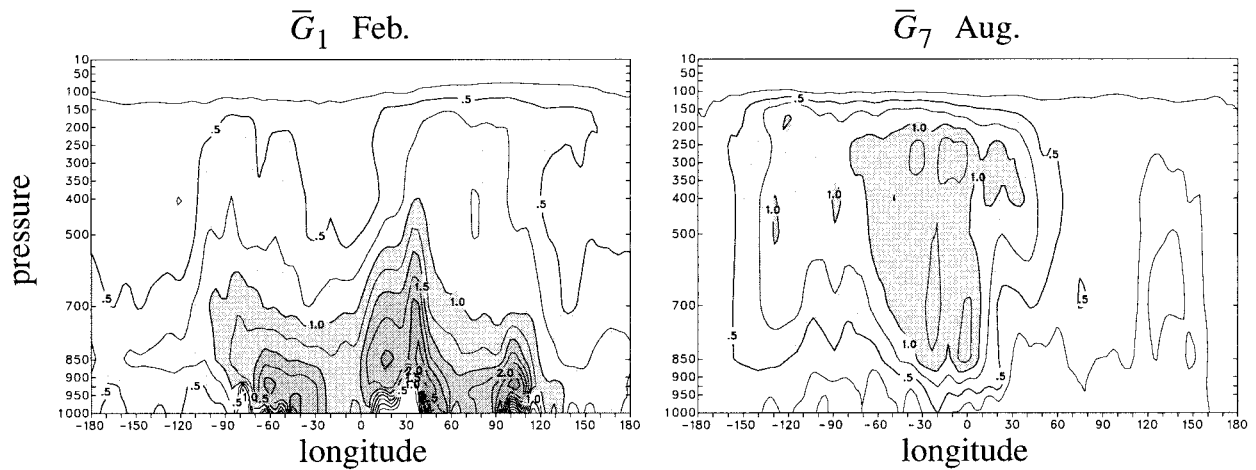

0.5   1.0   1.5   2.0

FIG. 10. Equatorial east–west section of the ensemble and monthly averaged Green function, for the month following the source month. The contour interval is 0.25 in units of G_∞.

in (21) to establish the time it takes for an individual pulse to result in eddy fluxes, and the magnitude of this contribution to the stationary-state fluxes.

Figure 14 shows the vertically integrated mean-motion and eddy fluxes for $G_{E,1}$ and $G_{E,7}$ (EUR source) as a function of lag time. The corresponding quantities for ENA (not shown) are virtually identical after ~3 months. As was the case for the stationary state, all terms are of the same order, with strong differences

in the mean-motion term between a winter and summer pulse related to the seasonal movement of the Hadley cell/monsoon. All terms are largest during the source month and in the vicinity of the source. After ~4 months, SH midlatitude transport is dominated by the transient eddies, with a smaller counteracting mean-motion contribution. In the SH midlatitudes both the transient-eddy and mean-motion terms peak at a lag of about 3–4 months, which is approximately
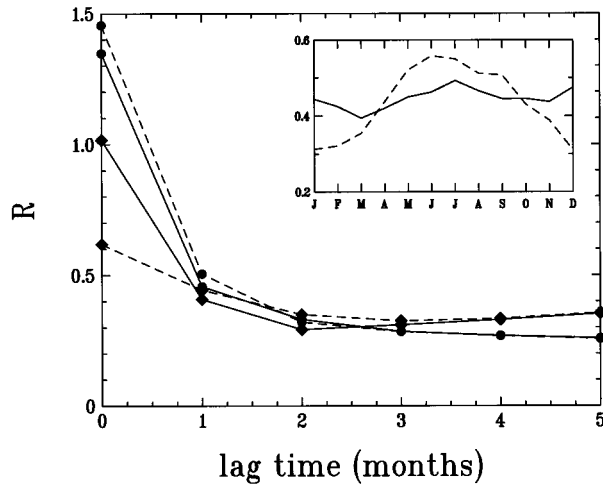
FIG. 11. The ratio, R, of parameterized to resolved vertical transport strengths, as defined in the text, for G_1 (diamonds) and G_7 (circles) for the EUR (dashed lines) and ENA (solid lines) cases. The inset shows R for the statistically stationary state during year 5 of the run with constant sources.

the time for G to reach 50% of its asymptotic value there (see Fig. 6).

The seasonality of the partition of $[\widetilde{\overline{vG}}]$ into its mean-motion and eddy components, at fixed lag, ξ, (not shown) is very similar to the seasonality of the partition of $[\widetilde{\overline{v\chi}}]$. The Green function is not constrained by (20), but obeys, after the source pulse has ceased, $\partial_y[\widetilde{\overline{vG}}] \cong -\partial_t[\widetilde{G}]$. The decay rate, $\partial_t[\widetilde{G}]$, has surprisingly little seasonality so that the transport partition of $[\widetilde{\overline{vG}}]$ at fixed ξ is very similar to that of $[\widetilde{\overline{v\chi}}]$ for constant source. When ξ is increased from one to several months, the amplitude of the seasonal cycle weakens while the overall pattern remains similar, except for the spreading south and the growing importance of the transient eddies in the SH.

Figure 15 shows the vertical structure of the eddy fluxes for the annual mean of the stationary state (EUR source) together with the monthly/ensemble means of $G_{E,1}$ and $G_{E,7}$ for the fourth month after injection. (The ENA case is qualitatively similar.) The fluxes, scaled in the vertical as for Fig. 9, are superposed on contours of the corresponding time/ensemble and zonally averaged mixing ratio. The standing eddies have significant amplitude only in the NH so that the smallness of their vertical integral in the SH (Figs. 13, 14) is not due to vertical cancellation. The standing eddies have strong seasonality in the Tropics (upward for the winter release, downward for the summer release). As already noted for the vertically integrated fluxes, the SH transient eddies of G at a lag of ~3 months make a large contribution to the eddies of the stationary state. Both for the stationary state and for G, there is a band of relatively high-amplitude transient eddies in the SH between about 30° and 60°S.

Note that in the SH the transient eddies are aligned to a large degree with the contours of the time-/ensem-

ble-mean, zonally averaged mixing ratio. That this is not merely an artifact of the plotting is confirmed by the fact that, where one sees the alignment, the transient eddies are inefficient in driving fluctuations (see below). This alignment, and the distribution of the transient eddies throughout the troposphere between ~30° and 60°S, first becomes evident at a lag of ~2 months and persists during the tropospheric homogenization phase of G (not shown). Eddy fluxes perpendicular to the mean gradient ("skew fluxes") represent effective advection of the mean mixing ratio in a flux-gradient parameterization of the eddies (Plumb and Mahlman 1987). For small amplitude fluctuations, skew fluxes can be interpreted as arising from Stokes drift (Plumb 1979). The details of the mechanism responsible for the flux alignment seen here remain to be explored.

7. Fluctuations

As the Green function is mixed by the atmosphere after the source pulse has ceased, ensemble fluctuations decay and the ensemble members converge to their common "climate." Here we focus on the structure and decay of these fluctuations.

First, we consider the fluctuations around the monthly and ensemble mean (the "pooled mean"), whose pooled variance is $\{\overline{G'^2}\}$, where $G' \equiv G - \{\overline{G}\}$. Because of the nonstationary nature of G, this variance has a slight positive bias compared to $\{\overline{G^{\dagger 2}}\}$, which is the monthly mean variance of the fluctuations, $G^{\dagger} \equiv G - \{G\}$, about the instantaneous ensemble mean. Nevertheless, we find that during the entire time evolution of G, the difference between the two variances, $\{\overline{G'^2}\} - \{\overline{G^{\dagger 2}}\} = \{G - \overline{G}\}^2$, is negligible, that is, $\{G - \overline{G}\}^2/\{\overline{G'^2}\} \ll 1$. For compactness of notation we now continue to use an overbar for the combined monthly and ensemble average.

Figure 16a shows the vertically integrated and horizontally averaged pooled variance as a function of time on a log–log plot. After a few months the variance decays approximately with a $t^{-3.5}$ power-law tail. Figure 16b shows the zonal average of the pooled variance to give an idea of its spatial structure. At early times the variance is highly concentrated in the region of the source, while after several months of decay, the variance, though of drastically reduced amplitude, has developed structure also in the upper atmosphere. In spite of its small amplitude, the large-lag variance does still contribute to the statistically stationary state in regions remote from the source (see below).

We now ask what role eddies play during the decay of variance. The averaged equation of motion for the fluctuations G' follows straightforwardly from (9) as

$$\overline{\partial_t G'^2} + \overline{\mathbf{v}} \cdot \nabla \overline{G'^2} + 2\overline{\mathbf{v}'G'} \cdot \nabla \overline{G} + \overline{\mathbf{v}' \cdot \nabla G'^2} + (\omega \text{ terms})$$
$$= 2\overline{G'\mathcal{D}'}, \qquad (22)$$

where the ω terms are of exactly the same form as those

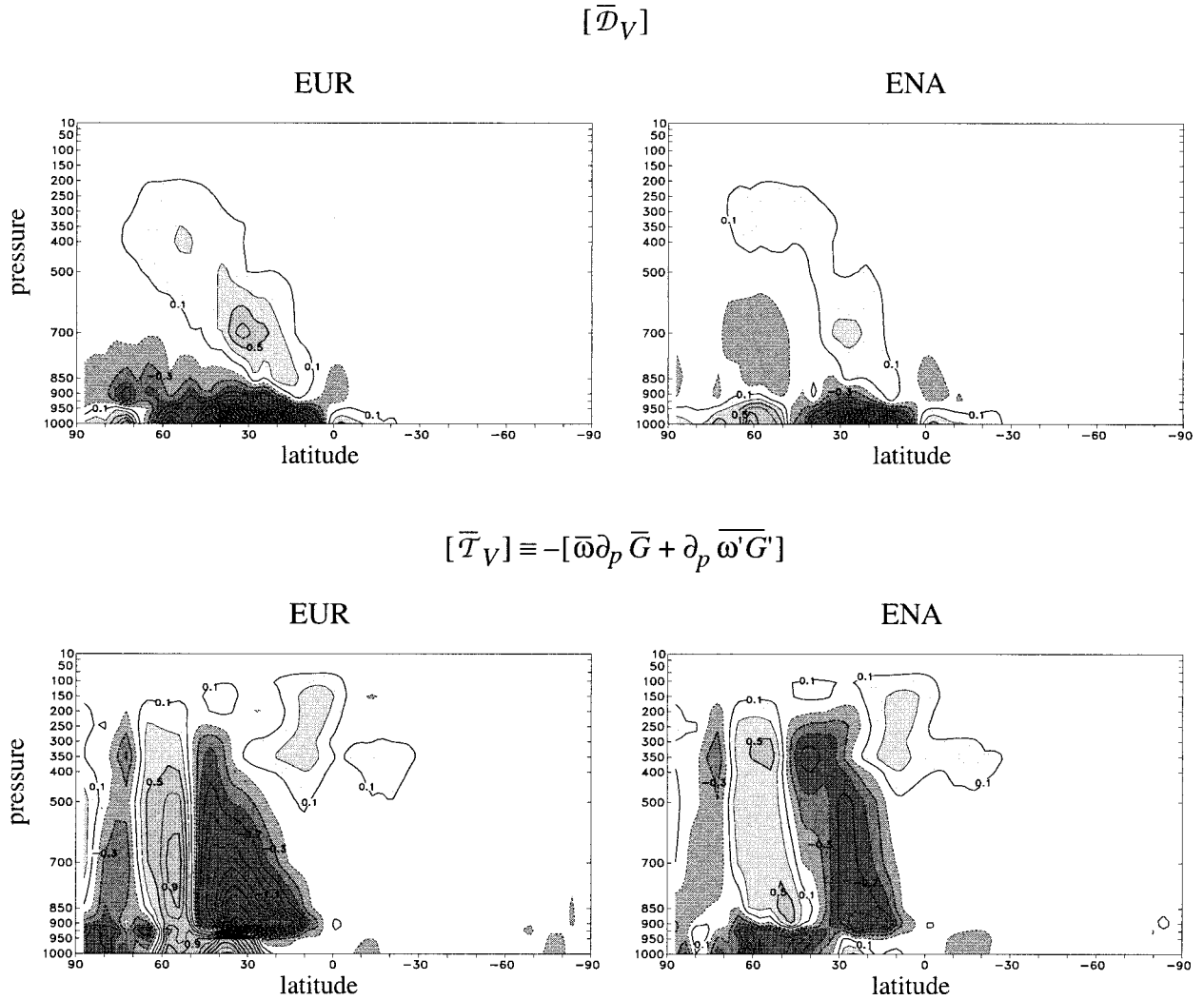# lag-1-month vertical transport "tendencies" (annual means)

$$[\overline{\mathcal{D}}_V]$$

EUR

ENA

$$[\overline{\mathcal{T}}_V] \equiv -[\overline{\omega}\partial_p \overline{G} + \partial_p \overline{\omega'G'}]$$

EUR

ENA

FIG. 12. Zonally averaged, annual- and ensemble-mean, lag-l-month parameterized vertical transport "tendency," $[\overline{\mathcal{D}}_V]$, and resolved vertical transport "tendency," $[\overline{\mathcal{T}}_V]$. All panels are plotted on the same scale with a contour interval of 0.2 in units of $10^{-6}\, G_\infty\, \mathrm{s}^{-1}$, straddling zero symmetrically.

involving $\mathbf{v}$ with the substitutions $\mathbf{v} \rightarrow \omega$ and $\nabla \rightarrow \partial_p$. In (22), $\mathcal{D} \equiv \mathcal{D}_H + \mathcal{D}_V$ and the triple correlations $\overline{\mathbf{v'} \cdot \nabla G'^2}$ (and similarly for ω) are assumed to be small. The source pulse, $S_G \equiv \Delta_3(\mathbf{r} - \mathbf{r}_I)\Delta(t - t_m)$, does not appear on the rhs, because all ensemble members see the same pulse, which is constant during the averaging period of the first month and zero otherwise. The term $\overline{\mathbf{v'}G'} \cdot \nabla\overline{G}$ and its vertical counterpart are eddy conversion terms that generate fluctuations from the mean gradient. While S_G does not explicitly appear in (22), during the source month, ∇S_G maintains $\nabla\overline{G}$ in the eddy conversion term as can readily be seen by taking gradients of (9).

Zonal averages of the advection and eddy-conversion terms of (22) are shown in Fig. 17 at a lag of 1 and 6 months. At early times, advection and conversion are of the same order of magnitude and highly concentrated in the region where the source pulse occurred. As the mixing ratio becomes homogenized, conversion dominates over advection (though both terms decay). The panels for July are typical of the late stages of the variance decay. The eddy conversion term is negative definite in the zonal average and, therefore, acts as a source of $\overline{G'^2}$, which in the upper atmosphere has roughly the same pattern as the conversion term in the presence of the relatively weak advection. We find that to a good approximation $[\overline{\mathbf{v'}G'} \cdot \nabla\overline{G}] + [\overline{\omega'G'}\partial_p\overline{G}] \cong ([\overline{v'G'}], [\overline{\omega'G'}]) \cdot (a^{-1}\partial_\phi, \partial_p)[\overline{G}]$. The smallness of this term,

Seasonality of stationary state eddy fluxes

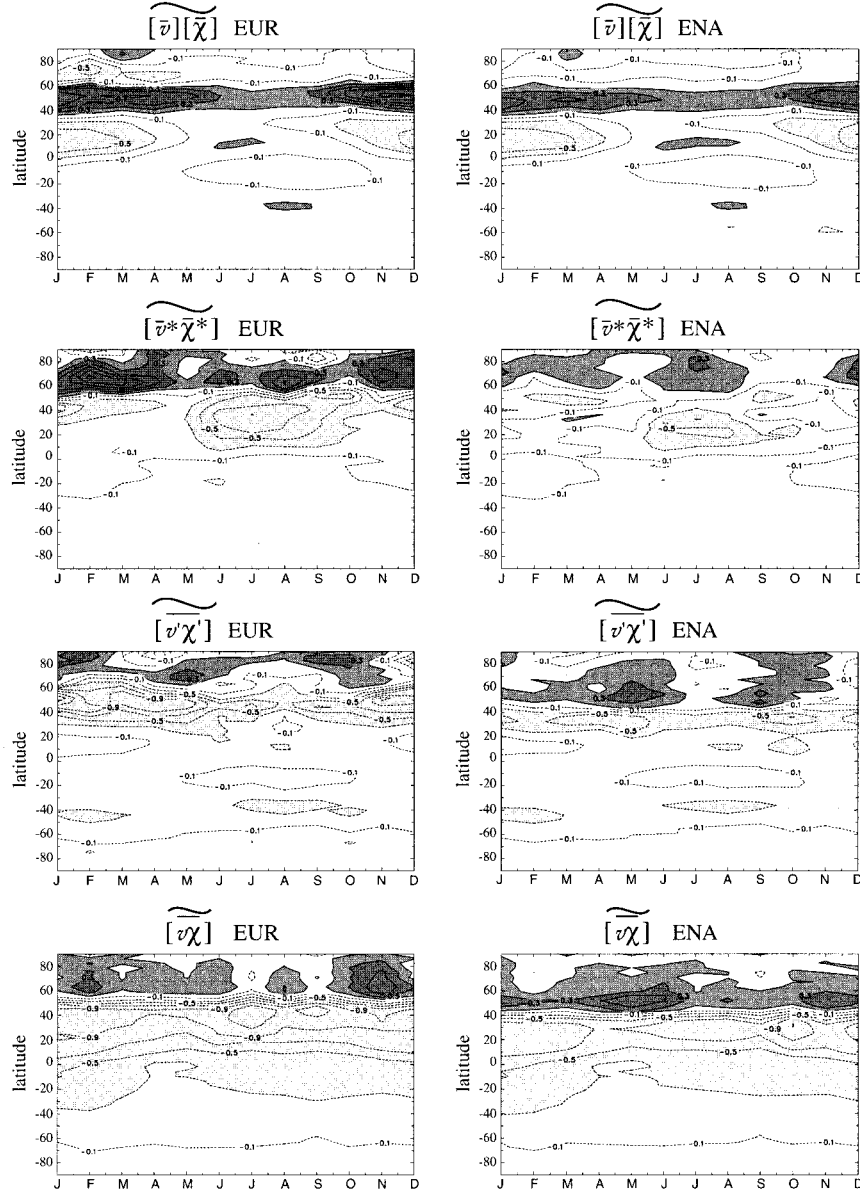FIG. 13. Vertically integrated mean-motion, standing-, and transient-eddy transport terms together with the total transport, $[\widetilde{\overline{v\chi}}]$, as a function of time for year 5 of the run with (right) constant EUR source, or (left) constant ENA source. The contour interval is 0.2, straddling zero symmetrically, in units of $5\sigma\langle\tilde{G}_\infty\rangle$ m s^{-1}. Northward transport (dark shades) is positive.

where the transient eddy fluxes are large in the SH (cf. Fig. 15), confirms that the transient-eddy fluxes there are approximately aligned with contours of constant $[\overline{G}]$ and hence inefficient in driving fluctuations.

The fluctuations, G', contribute to the fluctuations, χ', of the statistically stationary state for constant sources. Given a single source pattern of strength σ, the pooled variance of mixing ratio for month m can be written from (10) as

$$\overline{\chi'^2}/\sigma^2 = \sum_{k,n=0}^{\infty} \overline{G'_{m-k}G'_{m-n}}. \qquad (23)$$

A segment of the globally integrated lagged autocovariance matrix, $\overline{G'_{m-k}G'_{m-n}}$, is shown in Table 1. The diagonal lag-0 and lag-1 matrix elements ($k = n = 0$, 1) are by far the largest and capture the basic structure of $\overline{\chi'^2}$ (not shown). However, to capture the amplitude and pattern of $\overline{\chi'^2}$ in the remote upper atmosphere, the
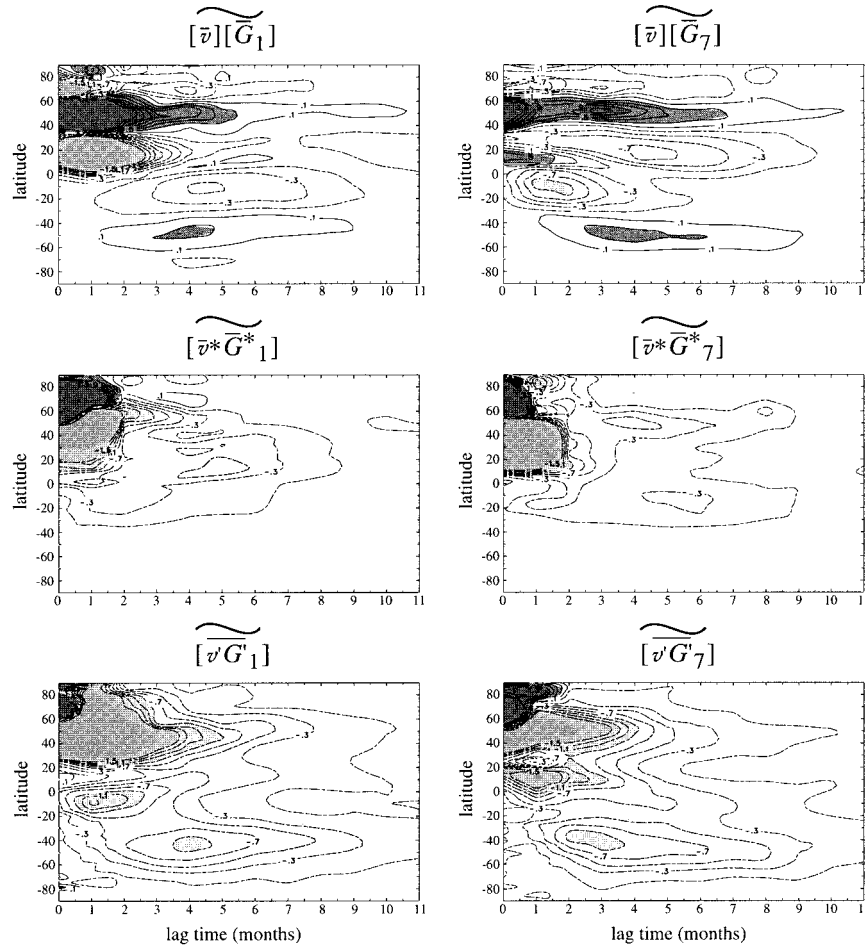
Eddy terms of G, EUR

$[\overline{v}][\widetilde{\overline{G}_1}]$

$[\overline{v}][\widetilde{\overline{G}_7}]$

$[\widetilde{\overline{v}*\overline{G}^*}_1]$

$[\widetilde{\overline{v}*\overline{G}^*}_7]$

$[\widetilde{\overline{v'G'}}_1]$

$[\widetilde{\overline{v'G'}}_7]$

FIG. 14. Vertically integrated mean-motion, standing- and transient-eddy transport terms of G as a function of lag time in months, including the source month as month 0, for (right) G_1 and (left) G_7. Contours are plotted from -1.5 to $+1.5$ with an interval of 0.2 in units of $0.2 \langle \tilde{G}_\infty \rangle$ m s^{-1}. Northward transport (dark shades) is positive.

off-diagonal matrix elements cannot be neglected in (23). The lag-6 diagonal term of Fig. 16b shows that, as expected, remote upper-level variance features come from large lag.

To take a direct look at ensemble fluctuations without monthly averaging, we have analyzed them for the 6-hourly time series of the vertically integrated Green function, $\tilde{G}$, and its flux, $\widetilde{\mathbf{v}G}$. From (9) it follows that the instantaneous ensemble variance of $\tilde{G}$ obeys

$$\frac{1}{2}\partial_t\{\tilde{G}^{\dagger 2}\} + \{\tilde{G}^{\dagger}\mathbf{\nabla}\cdot\widetilde{\mathbf{v}G^{\dagger}}\} = \{\tilde{G}^{\dagger}\tilde{\mathcal{D}}_H^{\dagger}\}. \quad (24)$$

The source pulse does not appear explicitly in (24) for the same reasons it did not appear in (22). Because of the very small size of our ensemble, the terms of (24) need to be averaged in some way so that as many independent statistical samples as possible are included in the average. We find that zonal and global averages

give reasonable results as judged by examining them for different source months and hence different ensembles of Gs.

Figure 18 shows the global averages of the variance, its dynamic generation term, $\{\tilde{G}^{\dagger}\mathbf{\nabla}\cdot\widetilde{\mathbf{v}G^{\dagger}}\}$, and dissipation term, $\{\tilde{G}^{\dagger}\tilde{\mathcal{D}}_H^{\dagger}\}$, for $\tilde{G}_{E,1}$ (EUR) as a function of time. [The dissipation term is computed from the other terms via (24).] The aspects about to be considered are very similar for other source months and the ENA case. The ensemble variance, $\{\tilde{G}^{\dagger 2}\}$, is a measure of the degree to which a different realization of the transport operator results in a different $\tilde{G}$. As seen in Fig. 18a, $\langle\{\tilde{G}^{\dagger 2}\}\rangle$ grows rapidly from zero to a quasi-stationary value after $\sim$10 days when the dissipation and generation terms come into approximate balance (Fig. 18b). Variance can be sustained only while the source is "on" maintaining gradients from which fluctuations can be generated. As soon as the source ceases, $\langle\{\tilde{G}^{\dagger 2}\}\rangle$ decays

EUR

statistically stationary state eddies (annual mean)

$([\bar{v}^*\bar{\chi}^*], -[\bar{\omega}^*\bar{\chi}^*])$ and $[\bar{\chi}]$ $([\overline{v'\chi'}], -[\overline{\omega'\chi'}])$ and $[\bar{\chi}]$
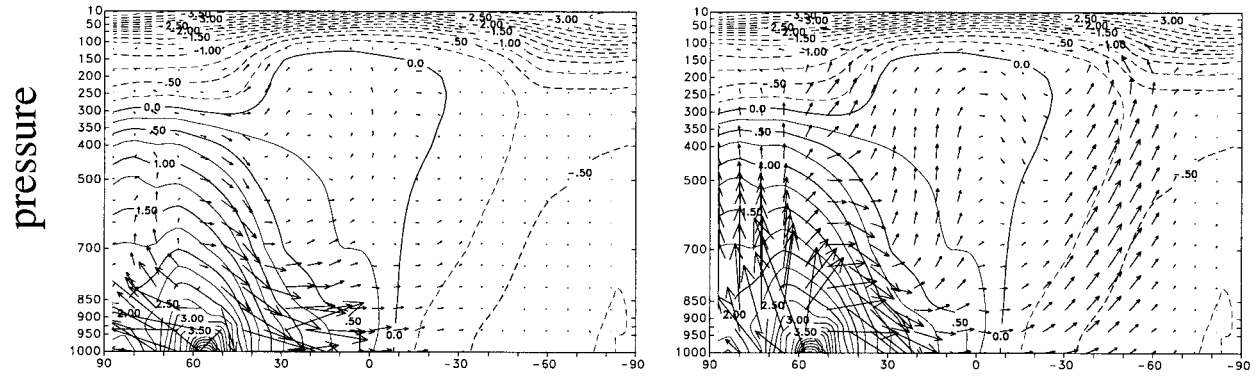
eddy contributions of G_1 , Apr.

$([\bar{v}^*\overline{G}^*], -[\bar{\omega}^*\overline{G}^*])$ and $[\overline{G}]$ $([\overline{v'G'}], -[\overline{\omega'G'}])$ and $[\overline{G}]$
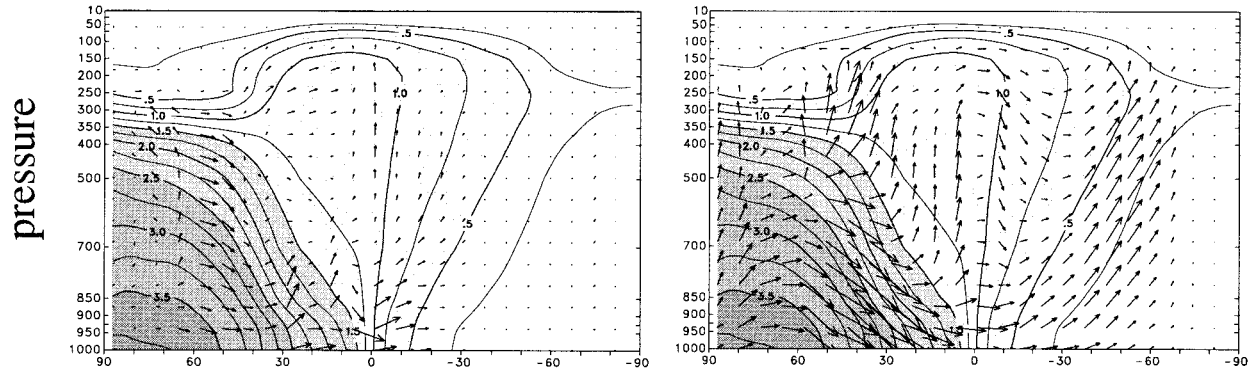
eddy contributions of G_7 , Oct.

$([\bar{v}^*\overline{G}^*], -[\bar{\omega}^*\overline{G}^*])$ and $[\overline{G}]$ $([\overline{v'G'}], -[\overline{\omega'G'}])$ and $[\overline{G}]$
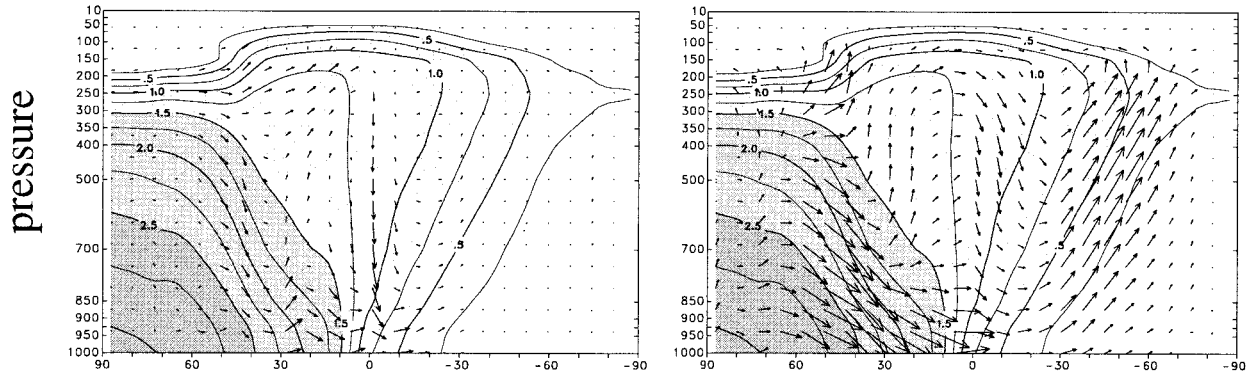
latitude $\longrightarrow$ latitude

FIG. 15. Standing and transient eddy fields (vectors) for the EUR source superposed on contours of the corresponding mean mixing ratio. For the statistically stationary state the horizontal flux vector scale is in units of σG_∞ m s^{-1}. For G_1 and G_7, ensemble and monthly averages are shown for the fourth month after release, with a horizontal flux vector scale in units of G_∞ m s^{-1}. The vertical components of the fluxes have been scaled as described in the text.
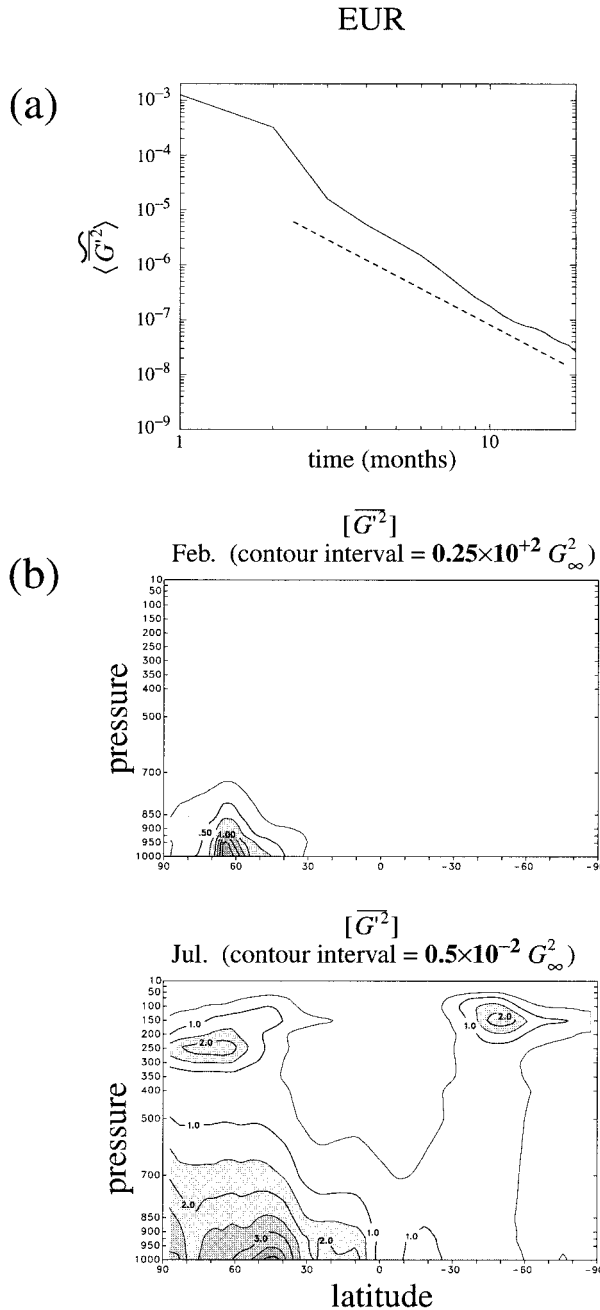
EUR

(a)

(b)

$[\overline{G'^2}]$
Feb. (contour interval = **0.25×10⁺² G_∞^2**)

$[\overline{G'^2}]$
Jul. (contour interval = **0.5×10⁻² G_∞^2**)

FIG. 16. (a) The vertically integrated, horizontally averaged pooled variance of G_1 in units of $\langle \tilde{G}_\infty \rangle^2$ m² kg⁻¹ as a function of time in months, with month 1 corresponding to January. The dashed line indicates a t^{-3} power law. (b) Zonal averages of the pooled variance of G_1 (units as indicated).

sharply as it becomes quickly inefficient to generate fluctuations from a field that is increasingly smooth due to dissipation. Log–log plots of the decaying tail of $\langle \{ \tilde{G}^{\dagger 2} \} \rangle$ reveal an approximate t^{-3} power-law decay, suggestive of "turbulent diffusion" (see inset of Fig. 18a).

Figure 18b shows that $-\langle \{ \tilde{G}^\dagger \tilde{\mathcal{D}}_H^\dagger \} \rangle$ resembles very

closely $\langle \{ \tilde{G}^{\dagger 2} \} \rangle$ plus some high-frequency noise. The linear correlation coefficient of the two curves is $r_c = 0.965$ and the correlation persists into the tail, with $r_c \gtrsim 0.9$ even when the first 60 days are omitted. For the global integrals, we can, therefore, write the dissipation term as a linear damping of the variance; that is,

$$\langle \{ \tilde{\mathcal{D}}_H^\dagger \tilde{G}^\dagger \} \rangle \simeq -\frac{1}{\tau_{\mathcal{D}}} \langle \{ \tilde{G}^{\dagger 2} \} \rangle. \qquad (25)$$

A least squares fit gives $\tau_{\mathcal{D}} \sim 10$ days ($\tau_{\mathcal{D}} = 11.2$, 11.3, 8.86, and 10.6 days, for $G_{E,1}$, $G_{E,7}$, $G_{A,1}$, $G_{A,7}$, respectively). Since the early time growth of variance is limited by the dissipation term, it is not surprising that τ_D is on the same order as the time to reach saturation. The $\sim t^{-3}$ decay of the tail, in spite of the linear damping (25), implies that the decay of variance under stationary turbulent advection takes place in a regime where the dynamical generation and dissipation terms attempt to balance.

In the context of homogeneous isotropic turbulence, tracer variance can certainly decay with a power law. A direct-interaction-approximation closure for the tracer two-point correlation function predicts that the tracer variance $\{ \chi^{\dagger 2} \} \sim R^{-d}(t)$, where the tracer integral scale $R(t)$ may be interpreted as the rms separation of two Lagrangian particles, and $d = 2$ or 3 is the spatial dimension (Kraichnan 1966; Lesieur and Herring 1985). Under conditions of a (kinetic) energy cascade ($d = 3$), or inverse energy cascade ($d = 2$), a Richardson law applies for which $R \sim t^{-3/2}$ giving $\{ \chi^{\dagger 2} \} \sim t^{-9/2}$ for $d = 3$, or $\sim t^{-3}$ for $d = 2$. For the enstrophy cascade regime ($d = 2$), the existence of a power law is not clear (e.g., Lesieur 1987). Unfortunately, it is not clear that these predictions apply directly to the atmosphere, where the kinetic energy does have an inverse cascade, but the global spectrum does not show a $k^{-5/3}$ range (Boer and Shepherd 1983), which is needed for the t^{-3} prediction. A $k^{-5/3}$ range might exist in a regional sense, but at present we merely note that a t^{-3} decay of variance can occur in 2D turbulence, and regard the $\sim t^{-3}$ decay seen in the model atmosphere as an empirical result.

To get an idea of the spatial structure of the terms of (24), we examined 6-h time series of zonal averages and maps of 30-day time averages (not shown). There is considerable spatial correlation between the dissipation and variance terms, particularly during the source month when northward-propagating structures leave the source (at phase speeds of ~ 1000 and ~ 500 km day⁻¹, for ENA and EUR, respectively). Maps of 30-day averages indicate that variance and dissipation are collocated with $\{ \tilde{G} \}$.

8. Summary and conclusions

The central theme of this paper was the study of passive tracer transport in terms of the climate of the transport Green function. Our goal was not to characterize
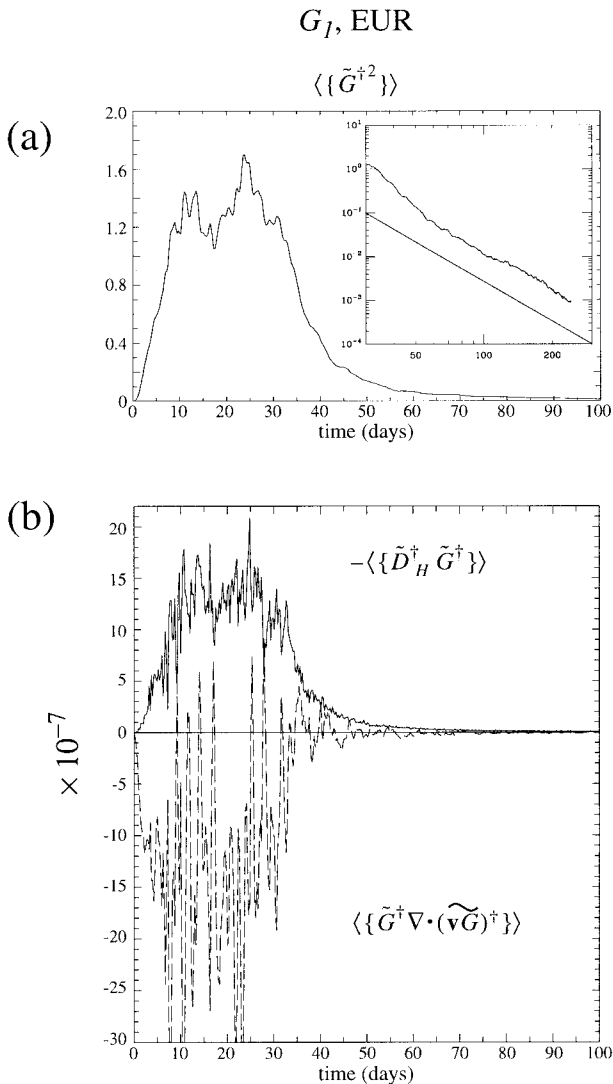
EUR

$$([\bar{\mathbf{v}} \bullet \nabla \overline{G'^2}] + [\bar{\omega}\partial_p \overline{G'^2}])/2 \qquad [\overline{\mathbf{v'}G'} \bullet \nabla \overline{G}] + [\overline{\omega'G'}\partial_p \overline{G}]$$

Feb. (contour interval = 10^{-5} G_∞^2 s^{-1}) Feb. (contour interval = 10^{-5} G_∞^2 s^{-1})

Jul. (contour interval = 10^{-8} G_∞^2 s^{-1}) Jul. (contour interval = 10^{-8} G_∞^2 s^{-1})

latitude latitude

FIG. 17. Zonal averages of the advection and eddy conversion terms for the pooled variance of G_1. The contour interval indicated straddles zero symmetrically.

the transport of any specific tracer, but to use a generic passive tracer to probe atmospheric transport. We exploited the linearity of passive tracer continuity to define a numerically tractable coarse-grained Green function, G, for two source locations (EUR and ENA) of interest

for anthropogenic emissions. The part of the coarse-grained Green function relevant for these sources was obtained through direct simulation of unit mass injections for an ensemble of three runs, using CCC GCMII. The Green function was then systematically character-

TABLE 1. The "small-lag corner" of the globally integrated lagged autocovariance matrix $\overline{G'_{m-k}G'_{m-n}}$ for $m = 12$ (Dec). The matrix elements have been normalized by the zero-lag variance element ($k = n = 0$).

n \ k	0	1	2	3	4	5	6
0	1.0000	−0.0798	−0.0027	−0.0024	−0.0015	−0.0009	−0.0007
1		0.2943	0.0143	0.0090	0.0057	0.0037	0.0027
2			0.0098	0.0053	0.0034	0.0023	0.0017
3				0.0033	0.0022	0.0016	0.0012
4					0.0016	0.0012	0.0009
5						0.0009	0.0007
6							0.0005

G_1, EUR

$\langle\{\tilde{G}^{\dagger 2}\}\rangle$

(a)

time (days)

(b)

$-\langle\{\tilde{D}^{\dagger}_H\tilde{G}^{\dagger}\}\rangle$

$\langle\{\tilde{G}^{\dagger}\nabla\cdot\widetilde{(\mathbf{v}G)^{\dagger}}\}\rangle$

$\times 10^{-7}$

time (days)

FIG. 18. (a) Six-hourly time series of the globally averaged ensemble variance $\langle\{\tilde{G}^{\dagger 2}\}\rangle$ for G_1, EUR, in units of $\langle\tilde{G}_\infty\rangle^2$. (The source pulse lasts from $t = 0$ to day 31.) The inset shows a log–log plot of $\langle\{\tilde{G}^{\dagger 2}\}\rangle$ for $t \geq 30$ days, with a straight line indicating a t^{-3} power law. (b) Corresponding 6-hourly values of the dissipation term, $\langle\{\tilde{\mathcal{D}}^{\dagger}_H\tilde{G}^{\dagger}\}\rangle$ (solid line), and the dynamical source term, $\langle\{\tilde{G}^{\dagger}\nabla\cdot\widetilde{\mathbf{v}G}^{\dagger}\}\rangle$ (dashed line), in units of $\langle\tilde{G}_\infty\rangle^2$ s^{-1}. Spikes of $\langle\{\tilde{G}^{\dagger}\nabla\cdot\widetilde{\mathbf{v}G}^{\dagger}\}\rangle$ that have been cut off for clarity do not exceed $-45 \times 10^{-7} \langle\tilde{G}_\infty\rangle^2$ s^{-1}.

ized in terms of its ensemble mean, or climate, and the structure and decay of fluctuations about this mean as the initial injection of tracer is mixed throughout the atmosphere. The climate of G is naturally suited to the identification of transport timescales, pathways, and mechanisms.

Transport timescales were identified by parameterizing the time evolution of G at a point in terms of three timescales and an overshoot measure. The time, $\tau_\infty(0.1)$, to get within 10% of the asymptotic value of G_∞, exceeds 1 yr at high-latitude lower levels. The other timescales

$\tau_0(\gamma)$ and $\tau_{\max}$ can be interpreted as arrival times (the time when G first reaches γG_∞, and $G_{\max}$, respectively). The model's two-box interhemispheric exchange time is ~0.6 yr for the sources studied. This two-box time has a direct connection with an integral time, τ^*, again based on the time-evolution of G (see apendix). We note that G here is a different object than the age spectrum of Hall and Plumb (1994), which is a propagator of boundary conditions. Tracer age can also be formulated in terms of G, and the connection between G and the age spectrum will be the subject of a future study.

Transport pathways and their seasonality were determined from the time-evolving climate of G. EUR and ENA tracers follow different pathways during the first few months, but then converge to a common distribution as mixing ratio is zonally homogenized. After ~3 months, differences between the EUR and ENA column burdens and vertically integrated fluxes become negligible. The main distinguishing characteristic between the two source cases is that EUR tracer is advected over the Asian continent, where continental conditions confine it to low levels and high latitudes in winter, while subjecting it to strong convection in summer. ENA tracer is advected over the Atlantic and consequently experiences more vertical transport in winter and less of a seasonal contrast. The zonally averaged evolution of G is largely consistent with the general picture given by Plumb and Mahlman (1987) and Plumb and McConalogue (1988). A "slope equilibrium" in which contours have reached approximately constant shape, while gradients continue to get flattened as $G \rightarrow G_\infty$, is established ~4 months after injection.

We investigated how much of the climate Green function's transport is due to eddies, what the structure of these eddies is, and how the eddy fluxes of the statistically stationary state with constant sources are synthesized from the corresponding eddy terms of G. Mean-motion, standing-eddy, and transient-eddy fluxes are all of the same order of magnitude but do not contribute equally everywhere. Southern Hemisphere transport is dominated by transient eddies established from tracer injected ~4 month earlier. The SH transient eddies extend vertically throughout much of the troposphere and are aligned to a large degree with contours of the zonally averaged mixing ratio. Waning tropical mean-motion southward transport in summer, associated with the seasonal movement of the Hadley cell and the monsoon, is largely compensated by increased standing-eddy transport.

The fluctuations of G about its climatic mean were characterized in terms of their spatial structure and their decay with time after injection (the fundamental self-averaging of G). While the source is "on," fluctuations of G are driven by mean gradients maintained by the source. Thereafter, fluctuations decay with a power law and the (itself decaying) source of pooled variance is the eddy conversion term. For large lag, eddy conversion dominates over advection. Ensemble fluctuations

were studied directly for the column burden, $\tilde{G}$. In terms of global averages, the dissipation term, $\langle\{\tilde{\mathcal{D}}_H^\dagger\tilde{G}^\dagger\}\rangle$, acts as a linear damping of the ensemble variance, $\langle\{\tilde{G}^{\dagger 2}\}\rangle$ with a timescale of ~10 days. After the source ceases, $\langle\{\tilde{G}^{\dagger 2}\}\rangle$ decays with an approximate t^{-3} power law suggestive of turbulent diffusion.

Since G was generated using CCC GCMII, we addressed the natural question: What is the relative importance of parameterized versus resolved transport. The resolved ($\mathcal{T}_V$) and parameterized ($\mathcal{D}_V$) vertical transports are of the same order of magnitude in terms of a globally integrated measure, with $\mathcal{D}_V$ dominating during the source month and $\mathcal{T}_V$ dominating thereafter. Close to the surface $\mathcal{D}_V$ removes tracer from the boundary layer where it dominates $\mathcal{T}_V$. Although even with a simple convective adjustment scheme, $\mathcal{D}_V$ contains some representation of deep convection (especially for the EUR case), upper-level vertical transport is dominated by $\mathcal{T}_V$.

Although our results are based on a model atmosphere, we hope that they are at least qualitatively representative of the real atmosphere. While validation of tracer transport is difficult because of a current lack of tropospheric upper-air measurements of quasi-passive, long-lived tracers [a situation that is improving (Maiss 1996, personal communication; Ray 1997, personal communication)], CCC GCMII has been intercompared with other models and validated against surface observations of SF_6 (Denning et al. 1997). The general transport pathways, the nature of the homogenization of G, the role of eddy transport, and the way in which ensemble fluctuations decay should all be robust features of tropospheric transport not overly sensitive to model formulation. Details of these features, such as the precise values of timescales, may well change as GCMs evolve and become more constrained by tracer observations.

The climate Green function provides a natural framework for the analysis of transport pathways, mechanisms, and timescales for sources with general time dependence, including constant sources leading to a statistically quasi-stationary state. Tracers that are subject to volume distributed source–sink terms not considered here, but have no feedback on the atmosphere, are also amenable to a Green function analysis.

APPENDIX

Integral Time and Connection to Stationary State

The integral time τ^* is defined such that $\int_0^t G(\xi)\,d\xi \to (t - \tau^*)G_\infty$ as $t \to \infty$. More precisely, we define $\tau^* = \lim_{t\to\infty}\hat{\tau}$, where

$$\int_0^t G(\xi)\,d\xi \equiv (t - \hat{\tau})G_\infty, \qquad (A1)$$

so that

$$\tau^* = \lim_{t\to\infty}\left(t - \frac{1}{G_\infty}\int_0^t G(\xi)\,d\xi\right). \qquad (A2)$$

With this definition, if $\tau^* \leq 0$, then G overshoots G_∞. Where $\tau^* \gg 0$, any overshoot is unlikely, G reaches G_∞ from below, and τ^* has a natural interpretation as an effective arrival time akin to $\tau_0(\frac{1}{2})$ (cf. Figs. 5 and 6).

For a time-independent source $S(\mathbf{r})$, the mixing ratio, χ, involves a time integral of G which from (27) can be written in terms of τ^*:

$$\chi(\mathbf{r}, t) = \int d^3r'\,S(\mathbf{r}')\int_0^t d\xi\,G(\mathbf{r}, t\,|\,\mathbf{r}', t - \xi)$$

$$= tG_\infty\int d^3r'\,S(\mathbf{r}') - G_\infty\int d^3r'\,S(\mathbf{r}')\tau^*(\mathbf{r}, \mathbf{r}'), \qquad (A3)$$

where we assume t is large enough to replace $\hat{\tau}$ with τ^*. The first term of (A3) is recognized as the linearly increasing spatially homogeneous background mixing ratio, χ_0, so that $\chi^+ \equiv \chi - \chi_0$ given by

$$\chi^+(\mathbf{r}, t) = -G_\infty\int d^3r'\,\tau^*(\mathbf{r}, \mathbf{r}')S(\mathbf{r}'). \qquad (A4)$$

In the case of a point source in the NH, $S(\mathbf{r}) = S_0\delta(\mathbf{r} - \mathbf{r}_0)$; we therefore have

$$\tau^* = -\frac{\chi^+}{G_\infty S_0}, \qquad (A5)$$

so that τ^* reduces simply to the scaled deviation of mixing ratio from the background. To compute τ_{2B}, we need to compute ΔM, which we can write in terms of χ^+ as

$$\Delta M = \int_{NH} d^3r'\,\chi^+ - \int_{SH} d^3r'\,\chi^+$$

$$= -2\int_{SH} d^3r'\,\chi^+, \qquad (A6)$$

so that τ_{2B} becomes

$$\tau_{2B} = \frac{4G_\infty}{\Delta S}\int_{SH} d^3r'\int d^3r''\,\tau^*(\mathbf{r}', \mathbf{r}'')S(\mathbf{r}''), \qquad (A7)$$

where $\Delta S \equiv \int_{NH} d^3r'\,S - \int_{SH} d^3r'\,S$. This expression again becomes very simple for the case of a point source in the NH:

$$\tau_{2B} = 2\frac{\langle\tilde{\tau}^*\rangle_{SH}}{\langle p_s\rangle/g} = \frac{\langle\tilde{\tau}^*\rangle_{SH} - \langle\tilde{\tau}^*\rangle_{NH}}{\langle p_s\rangle/g}, \qquad (A8)$$

where $\langle \ldots \rangle_{NH}$ and $\langle \ldots \rangle_{SH}$ denote hemispheric area averages over the NH and SH.

We have suppressed the dependence of G (and, therefore, of τ^*) on source time, t', here to keep the equations as simple as possible. The dependence of $G(t', \xi)$ on t' can be dealt with, for example, via Fourier transform on t'. In this sense, the above discussion is valid for the annual mean of G over t' (at fixed lag, ξ).

REFERENCES

Boer, G. J., 1982: Diagnostic equations in isobaric coordinates. *Mon. Wea. Rev.,* **110,** 1801–1820.

——, and T. G. Shepherd, 1983: Large-scale two-dimensional turbulence in the atmosphere. *J. Atmos. Sci.,* **40,** 164–184.

Bowman, K. P., and P. J. Cohen, 1997: Interhemispheric exchange by seasonal modulation of the Hadley circulation. *J. Atmos. Sci.,* **54,** 2045–2059.

Corrsin, S., 1951: On the spectrum of isotropic temperature fluctuations in isotropic turbulence. *J. Appl. Phys.,* **22,** 469–473.

Denning, A. S., and Coauthors, 1997: Three-dimensional transport and concentration of SF_6: A model intercomparison study (TransCom 2). *Tellus,* in press.

Enting, I. G., C. M. Trudinger, and R. J. Francey, 1995: A synthesis inversion of the concentration and $\delta^{13}C$ of atmospheric CO_2. *Tellus,* **47B,** 35–52.

Fung, I., K. Prentice, E. Matthews, J. Lerner, and G. Russell, 1983: Three-dimensional tracer model study of atmospheric CO_2: Response to seasonal exchanges with the terrestrial biosphere. *J. Geophys. Res.,* **88,** 1281–1294.

Gollub, J., J. Clarke, M. Gharib, B. Lane, and O. Mesquita, 1991: Fluctuations and transport in a stirred fluid with a mean gradient. *Phys. Rev. Lett.,* **67,** 3507–3510.

Hall, T. M., and R. A. Plumb, 1994: Age as a diagnostic of stratospheric transport. *J. Geophys. Res.,* **99,** 1059–1070.

Harnisch, J., R. Borchers, P. Fabian, and M. Maiss, 1996: Tropospheric trends of CF_4 and C_2F_6 since 1982 derived from SF_6 dated stratospheric air. *Geophys. Res. Lett.,* **23,** 1099–1102.

Jacob, D. J., M. J. Prather, S. C. Wofsy, and M. B. McElroy, 1987: Atmospheric distribution of ^{85}Kr Simulated with a general circulation model. *J. Geophys. Res.,* **92,** 6614–6626.

——, and Coauthors, 1997: Evaluation and intercomparison of global atmospheric transport models using ^{222}Rn and other short-lived tracers. *J. Geophys. Res.,* **102,** 5953–5970.

Kraichnan, R. H., 1966: Dispersion of particle pairs in homogeneous turbulence. *Phys. Fluids,* **9,** 1937–1943.

——, 1974: Convection of a passive scalar by a quasi-uniform random straining field. *J. Fluid Mech.,* **64,** 737–762.

Levin, I., and V. Hesshaimer, 1996: Refining of atmospheric transport model entries by the globally observed passive tracer distributions of ^{85}krypton and sulfur hexafluoride (SF_6). *J. Geophys. Res.,* **101,** 16 745–16 755.

Lesieur, M., 1987: *Turbulence in Fluids.* 3d ed. Kluwer Academic, 515 pp.

——, and J. Herring, 1985: Diffusion of a passive scalar in two-dimensional turbulence. *J. Fluid Mech.,* **161,** 77–95.

McFarlane, N. A., G. J. Boer, J.-P. Blanchet, and M. Lazare, 1992: The Canadian Climate Centre second generation general circulation model and its equilibrium climate. *J. Climate,* **5,** 1013–1044.

Pierrehumbert, R. T., and H. Yang, 1993: Global chaotic mixing on isentropic surfaces. *J. Atmos. Sci.,* **50,** 2462–2480.

Plumb, R. A., 1979: Eddy fluxes of conserved quantities by small-amplitude waves. *J. Atmos. Sci.,* **36,** 1699–1704.

——, and J. D. Mahlman, 1987: The zonally averaged transport characteristics of the GFDL general circulation model. *J. Atmos. Sci.,* **44,** 298–327.

——, and D. D. McConalogue, 1988: On the meridional structure of long-lived tropospheric constituents. *J. Geophys. Res.,* **93,** 15 897–15 913.

——, and M. K. W. Ko, 1992: Interrelationships between mixing ratios of long-lived stratospheric constituents. *J. Geophys. Res.,* **97,** 10 145–10 156.

Prather, M. J., 1996: Time scales in atmospheric chemistry: Theory, GWPs for CH_4 and CO, and runaway growth. *Geophys. Res. Lett.,* **23,** 2597–2600.

——, M. McElroy, S. Wofsy, G. Russel, and D. Rind, 1987: Chemistry of the global troposphere: Fluorocarbons as tracers of air motion. *J. Geophys. Res.,* **92,** 6579–6613.

Rasch, P. J., 1994: Conservative shape-preserving two-dimensional transport on a spherical reduced grid. *Mon. Wea. Rev.,* **122,** 1337–1350.

Rayner, P. J., and R. M. Law, 1995: A comparison of modelled responses to prescribed CO_2 sources. CSIRO Division of Atmospheric Research Tech. Paper 36, 84 pp. [Available from CSIRO, Division of Atmospheric Research, PMB 1, Mordialloc 3195 Australia.]

Shraiman, B. I., and E. D. Siggia, 1994: Lagrangian path integrals and fluctuations in random flows. *Phys. Rev. E,* **49,** 2912–2927.